

SAND99-1255
Unlimited Release
Printed May 1999

Analysis of Z Pinch Shock Wave Experiments

Timothy Trucano and Kent G. Budge
Computational Physics Research and Development

Jeffery Lawrence
Target and Z-Pinch Theory

James Asay, Clint Hall, Kathleen Holland, and Carl Konrad
Shock Physics Applications

Wayne Trott
Energetic and Multiphase Processes

Gordon Chandler
Diagnostics and Target Physics

Kevin Fleming
Explosive Projects/Diagnostics

Sandia National Laboratories

P. O. Box 5800
Albuquerque, NM 87185-0819

Abstract

In this paper, we report details of our computational study of two shock wave physics experiments performed on the Sandia Z machine in 1998. The novelty of these particular experiments is that they represent the first successful application of VISAR interferometry to diagnose shock waves generated in experimental payloads by the primary X-ray pulse of the machine. We use the Sandia shock-wave physics code ALEGRA to perform the simulations reported in this study. Our simulations are found to be in fair agreement with the time-resolved VISAR experimental data. However, there are also interesting and important discrepancies. We speculate as to future use of time-resolved shock wave data to diagnose details of the Z machine X-ray pulse in the future.

Acknowledgment

We would like to thank Randy Summers and Allen Robinson for reviewing this report.

Sandia is a multiprogram laboratory operated by Sandia Corporation, a Lockheed Martin Company, for the United States Department of Energy under Contract DE-AC04-94AL85000.

Contents

1. Introduction	1
2. Experimental Summary	2
Wire Array, Hohlraum, and Payload Description	2
Drive Characterization	6
Discussion of VISAR Data	10
3. Calculations	11
Description of ALEGRA	11
Description of SPARTAN	12
Calculation Set-Up Information	15
Analysis of Shot Z189	16
Analysis of Shot Z190	22
Sensitivity Studies	28
4. Discussion	36
References	37
Appendix A	40
Appendix B	43
Listings for Z189	44
Listings for Z190	51

(This page left blank.)

Figures

- Figure 1. Photo of a typical wire array fielded on the Z machine.
- Figure 2. Schematic of secondary hohlraums which are used to drive shock EOS experiments on the Z machine. The primary hohlraum is approximately 1 cm in length.
- Figure 3. Schematic of EOS payloads for secondary hohlraum driven EOS experiments on the Z machine.
- Figure 4. Schematic of payload for shots Z189 and Z190. The schematic is not to scale. The payload is not axisymmetric with respect to the axis of the secondary hohlraum. Viewed axially, its cross section is that of a 0.6 cm by 0.4 cm rectangle. The alignment is such that the A sample depth is closest to the short side of the secondary hohlraum.
- Figure 5. Smoothed drive overlaid with raw data for Z189.
- Figure 6. Smoothed drive overlaid with raw data for Z190.
- Figure 7. Extrapolated drive below 30 eV for Z189 and Z190.
- Figure 8. Visar data for Z189 and Z190.
- Figure 9. Illustration of meshing used in our calculations (not to scale).
- Figure 10. Ablation velocities of selected mass elements for Z189.
- Figure 11. A t-x diagram for Z189. Motion prior to the arrival of the main shock appears to a depth of around 100 microns. The VISAR data collection depths are shown.
- Figure 12. Radiation temperature histories.
- Figure 13. Radiation temperature vs depth at peak drive time of 13.0 ns.
- Figure 14. Time histories of pressure as a function of initial depth in the sample.
- Figure 15. Pressures at diagnostic locations for Z189A and Z189B.
- Figure 16. Particle velocity attenuation for Z189.
- Figure 17. Computed particle velocity histories at the A and B locations for Z189.
- Figure 18. Comparison of computed and measured particle velocity histories at Z189A. The particle velocity non-peak error bars are smaller than the size of the symbols used for the experimental data.
- Figure 19. Comparison of computed and measured particle velocity histories at Z189B. 20
- Figure 20. Ablation velocities of selected mass elements for Z190.
- Figure 21. An x-t diagram for Z190. Motion prior to the arrival of the main shock appears to a depth of around 100 microns.
- Figure 22. Radiation temperature histories.
- Figure 23. Radiation temperature vs depth at peak drive time of 15.0 ns.
- Figure 24. Time histories of pressure as a function of initial depth in the sample.
- Figure 25. Pressures at diagnostic locations for Z189A and Z189B.
- Figure 26. Particle velocity attenuation for Z190.
- Figure 27. Computed particle velocity histories at the A and B locations for Z190.
- Figure 28. Comparison of computed and measured particle velocity histories at Z190A. The non-peak particle velocity error bars are smaller than the size of the symbols used for the experimental data.
- Figure 29. Comparison of computed and measured particle velocity histories at Z190B. The peak velocity error bar is off the scale of the plot.
- Figure 30. 18 versus 36 energy groups for Z189A. Triangles denote 36 groups.

- Figure 31. 18 versus 36 energy groups for Z189B. Triangles denote 36 groups.
- Figure 32. Comparison of calculations with for Z189A. Triangles correspond to ; crosses correspond to .
- Figure 33. Comparison of calculations with for Z189B. Triangles correspond to ; crosses correspond to .
- Figure 34. Baseline versus finer meshing for Z189A. Triangles are the finer meshed calculation.
- Figure 35. Baseline versus finer meshing for Z189B. Triangles are the finer meshed calculation.
- Figure 36. Z189A versus Z190A. Triangles are the ALEGRA calculation corresponding to Z190.
- Figure 37. Z189B versus Z190B. Triangles are the ALEGRA calculation corresponding to Z190.
- Figure 38. Baseline versus and 18 eV extrapolation for Z189A. Triangles correspond to the 18 eV extrapolation in the drive.
- Figure 39. Baseline versus and 18 eV extrapolation for Z189B. Triangles correspond to the 18 eV extrapolation in the drive.
- Figure 40. Possible hohlraum geometries of interest for EOS experiments.
- Figure 39. Calculated two-dimensional pressure histories for shot Z189. The indicated positions are the Lagrangian distances from the original front surface, and the multiple curves are for positions across the finite lateral dimension of the semi-infinite slab.
- Figure 39. Calculated two-dimensional velocity histories for shot Z189 for Lagrangian points 154 and 308 (m from the original front surface. The multiple curves are for different positions across the finite lateral dimension of the semi-infinite slab.

Tables

Table 1. Timing and particle velocity errors associated with Z189 and Z190.

(This page left blank.)

Executive Summary

This report discusses a computational study of two shock wave experiments, Z189 and Z190, performed on the Sandia Z Machine early in 1998. The Sandia shock wave physics code ALEGRA is used to perform the analysis. As such, these experiments provide a good opportunity to perform some validation of the radiation physics packages in ALEGRA.

In these experiments, a so-called "secondary" gold hohlraum was attached to the primary hohlraum typically utilized in Z machine drive experiments. The secondary hohlraum provided a radiative drive, estimated to peak at an effective black body temperature on the order of 80 eV. Each secondary hohlraum had an experimental package consisting of an aluminum sample instrumented to gather VISAR time-resolved shock wave profile data at two different sample depths in the aluminum. The detailed geometry and dimensions are provided in the body of the report, as well as a discussion of the radiative drive. Fairly large error bars in temperature (perhaps 10 or 20 percent) are believed to be associated with the time-dependent black body temperature of the drive, with these error bars increasing in size below apparent temperatures of approximately 30 eV.

A detailed discussion of the calculations is presented. The calculations performed in the report used the SPARTAN SP_N package of Morel and Hall, which was implemented in ALEGRA. The calculations are effectively one-dimensional. This restriction on our analysis is compatible with the goals of the experimental program, which were to generate useful uniaxial strain conditions in the samples that are typical of what is required to perform accurate equation of state and constitutive characterization experiments.

A careful comparison of calculations and experimental data is provided. The general conclusion of this analysis is that our calculations are in reasonable agreement with the data and their error bars, but the agreement is not excellent. While the calculations tend to lie (barely in some cases) within the error bars on the shock wave data, the error bars themselves are larger than desirable for precise equation of state work, for example. We used the occasion of this work to perform some sensitivity studies, in which we varied the treatment of the radiation energy group structure, the order of the SP_N treatment, the resolution of the mesh, and the radiative drive itself.

We discovered that, by far, the most important sensitivity in this computational analysis is radiative drive variability. Since very accurate determination of the time-dependent radiative drive in experiments like Z1899 and Z190 is still a goal of the Sandia Z program, these sensitivities suggest that we are currently limited in our ability to use these experiments fully for use in validating the radiation-hydrodynamics in ALEGRA. Nonetheless, these initial studies are quite encouraging, especially in our capability to perform such time-resolved shock diagnostics in the Z machine environment. The reasonable agreement that we have achieved suggests that these experiments should be used in the future for further studies as the ALEGRA radiation-hydrodynamics capabilities expand.

(This page left blank.)

Analysis of Z Pinch Shock Wave Experiments

1. Introduction

The Z machine at Sandia National Laboratories utilizes fast Z pinches to provide large amounts of near Planckian soft x-ray energy for varied purposes [1]. In this paper, we will discuss one of them - the generation of ablative shock waves for high pressure equation of state (EOS) studies. The Z machine EOS program is engaged in studying the limits and accuracy for material studies of the shock waves that can be generated by the Z machine x-ray pulse.

One of the most desirable features of the Z machine is the sheer quantity of x-ray energy that is available. Among other things, this means that one can work with larger experimental payload sizes. This eases the burden placed on accurate, time-resolved shock wave diagnostics. As well, there is the possibility of “staging” this energy creatively, both to better form shock waves as well as to allow the opportunity to create off-Hugoniot loading, such as isentropic compression states. For example, clever staging of the energy can conceivably be applied for the purpose of launching an intact flyer plate to hypervelocities. This type of plate can, itself, be used to generate shock waves, as well as to study hypervelocity impact phenomena. In certain geometries, the launching technique might also be used to generate and study interfacial hydrodynamic instabilities.

Time-resolved diagnostics associated with a generated shock wave may also provide a complementary diagnostic for x-ray drive characterization for Z machine experiments. The accuracy associated with VISAR data, in particular, may place stringent bounds on the quantitative characteristics of the drive. There is a definite need to improve drive characterization below certain temperature thresholds (for the experiments in this paper, on the order of approximately 30 eV), and the sharp details available by analyzing ablative shock wave propagation provide an attractive possibility.

Our focus in this report will be on a relatively straightforward application of the Z machine: the production, propagation, and diagnosis of ablative shock waves in aluminum. The particular experiments we consider, shots Z189 and Z190, were specifically intended for this purpose and represent the first truly successful time-resolved measurements of shock wave production and propagation on the Z machine. The goal of experiments such as these is to provide high quality and high accuracy simultaneous measurements of both shock wave velocity and particle velocity in experimental payloads. Simultaneous accurate measurement of these quantities directly determines the dynamic pressure and density in the payload, hence the necessary EOS information.

Shots Z189 and Z190 were more like diagnostic development experiments, in that the simultaneous measurements did not achieve accuracy great enough to be fully considered as EOS measurements, nor were they designed to. Fiber-optic active shock breakout diagnostics were fielded to perform direct high accuracy measurements of shock wave velocity. VISAR laser interferometry was fielded to perform *in situ* time-resolved particle velocity measurements simultaneously. Both of these techniques are in common use with the classic instrument of shock wave physics experiments - high velocity gun impacts. Neither one of these diagnostics has been fielded in a hostile environment such as the Z machine experimental area before. While there is still work to be done to make these techniques perform to as great a level of accuracy as we believe possible, we will see that the VISAR data that were measured on Z189 and Z190 have considerable interest.

Our analysis of these experiments provides information on two broad fronts. First, as is always the case, computational analysis of an experiment provides a great deal of information that improves our understanding of the experiment. Second, careful comparison of our calculations with the data from shots Z189 and Z190 is a code validation exercise of considerable value to us. We use the ALEGRA [3] shock wave physics code to perform our analysis of these experiments. The resulting experiment-code comparisons provide interesting data for validating the radiation-hydrodynamics capability in the code, as well as interesting insights into the functioning of the experiments.

In Section 2 we discuss some details associated with the experiments, including the energy “staging” scheme applied, discussion of the drive characterization, and presentation of the time-resolved data that were acquired on the experiments. We present ALEGRA simulations of these experiments in Section 3. There, we briefly review this shock wave physics code, present some detailed information regarding the radiation-transport algorithms, present baseline computations of the experiments, and perform some sensitivity studies of the baseline calculations. We discuss our conclusions from these analyses in Section 4. Appendix A discusses on use of 2-D calculations for analysis of these experiments. Full listings of the necessary input for the baseline calculations are provided in Appendix B to this report.

2. Experimental Summary

Wire Array, Hohlraum, and Payload Description

A good recent reference which discusses fast Z-pinch formation and radiative output on the Sandia Z machine is the article of Spielman, *et al* [2]. The Z machine is a pulsed power machine which capacitively stores up to 11 MJ of energy in a bank of Marx generators. Fast switching techniques convert this energy into a current pulse of up to 20 MA peak, with a duration of on the order of 100 ns. This current is deposited in a *wire array*, an axisymmetric configuration of some hundreds of fine wires that is carefully constructed. The implosion of this array under the magnetic forces induced by the current flow produces the basic radiation pulse which is staged for use in the present EOS experiments. For experiments Z189 and Z190, this wire array consisted of three hundred 11.3 μm diameter

Analysis of Z Pinch Shock Wave Experiments

cylindrical tungsten wires, with an overall configuration diameter of 2.0 cm. The overall axial length of this wire array was 1.0 cm. A photo of a wire array is given in Figure 1.

The careful construction of the wire array, the use of high Z wire material, and the number of wires, as well as the speed of the magnetic implosion (the Z machine is called a *fast Z*-pinch machine) all contribute to reducing the growth rate of the MHD Rayleigh-Taylor instability. The resulting implosion produces an immensely strong, time dependent pulse of X-ray radiation, with perhaps 2 MJ or more of total X-ray energy delivered in a pulse width (Full-Width Half-Max) of between 5 and 10 nanoseconds typically. The resulting X-ray pulse has powers of up to 300 TW. Experiments Z189 and Z190 were somewhat conservative. Identical wire arrays were used, with conditions such as to produce approximately 120 TW radiation pulses.

The Z-pinch implosion typically takes place inside a gold coated (10 μm thick) hohlraum, mainly for the purpose of utilizing the created X-ray energy. This hohlraum is called the primary hohlraum in the following discussion. The high Z coating produces radiation re-emission phenomena that tend to thermalize a good part of the direct Z-pinch X-ray pulse. Among other things, this allows us to accurately approximate the time dependent radiation source as a Planckian, or blackbody, radiation source. The measured temperatures in primary hohlraums for the observed X-ray powers are 150 eV or more, dependent upon the hohlraum volume. For experiments Z189 and Z190, the primary hohlraum temperature was believed to peak at around 140 eV. This temperature was not directly measured on these experiments. However, the wire array and machine operating conditions were essentially identical to previous experiments where the primary hohlraum temperature was measured.

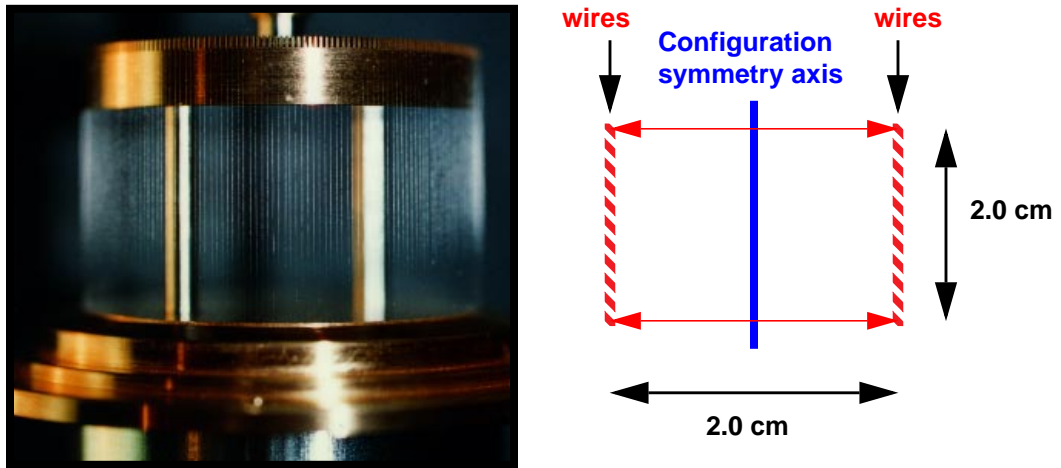


Figure 1. Photo of a typical wire array fielded on the Z machine.

Secondary hohlraums (similarly coated with gold) are fielded on these experiments. There is concern over payload preheat, from either energetic non-Planckian radiation or from energetic particles produced by the power conditioning and Z-pinch implosion, if experimental payloads were directly illuminated in the primary hohlraum. Secondary

Analysis of Z Pinch Shock Wave Experiments

hohlraums can be used to stage the basic Planckian primary hohlraum radiation to an experimental payload, while minimizing the opportunity for preheat. As we will discuss in our analysis, we believe that preheat was avoided on these experiments through the use of secondary hohlraums. The radiation drive in the secondary hohlraum is further thermalized, leading to a more Planckian source than seen in the primary hohlraum.

Another issue of concern, especially for EOS experiments, is uniformity of the radiation illumination of the experimental payload. This is, perhaps, an even more significant problem when we stage radiation using secondary hohlraums. The secondary hohlraums must be designed to provide sufficient uniformity for accurate EOS measurements. The basic design of secondary hohlraums for various applications is currently a research topic among the Z machine user community. We will say more about uniformity issues for Z189 and Z190 in our concluding remarks.

Reference 4 describes the experimental details for the EOS experimental setups. For purposes of the EOS program, experiments Z189 and Z190 used *tangential* secondary hohlraums. A schematic of the basic staged primary/tangential secondary hohlraums and payload assemblies for these experiments is presented in Figure 2. The secondary hohlraums themselves differed somewhat for the two experiments. Shot Z189 used a 0.6 cm long “short” side length. In addition, a 0.4 cm diameter diagnostic aperture was located on the short side for Z189. The short side length for Z190 was 0.8 cm. Parylene-N burnthrough foils were used in each experiment to remove or reduce the run-in radiation pulse associated with the Z-pinch. The thickness of this foil was 6.28 μm for shot Z189, 1.83 μm for Shot Z190. The foils were placed on the pinch side of the shine shield.

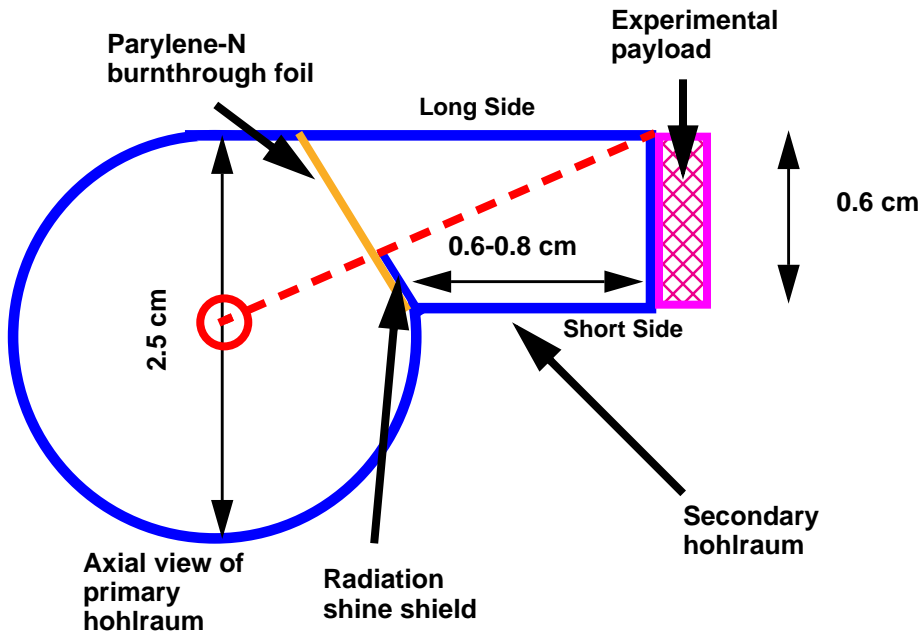


Figure 2. Schematic of secondary hohlraums which are used to drive shock EOS experiments on the Z machine. The primary hohlraum is approximately 1 cm in length.

Analysis of Z Pinch Shock Wave Experiments

For each experiment, there were actually two tangential secondary hohlraums of equal volumes. A fiber-optic active shock breakout diagnostic was applied in the alternate secondary hohlraum to measure the shock wave velocity. We will not discuss this diagnostic, or the collected data, in this report [4].

A general schematic of the payload geometry that was used in Z189 and Z190 is shown in Figure 3. We have shown the termination of the secondary hohlraum, labeled “Au”; the 99.5% pure 1100 aluminum sample; and a backing lithium fluoride laser window, which is characteristic of the VISAR time-resolved diagnostic [5-6].

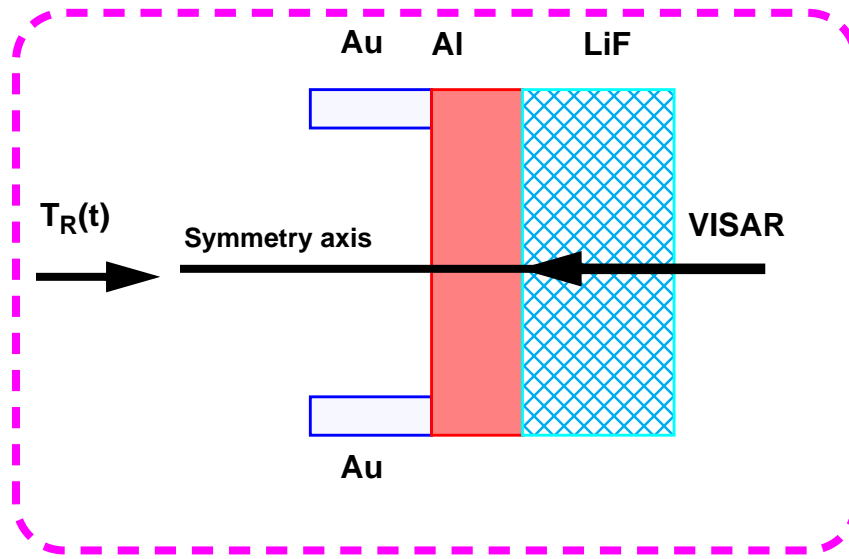


Figure 3. Schematic of EOS payloads for secondary hohlraum driven EOS experiments on the Z machine.

The payload for shots Z189 and Z190 is more specialized than that depicted in Figure 3. We show this payload in Figure 4. $T_R(t)$ defines the presence and direction of the radiation drive on the payload from the secondary hohlraum, which is applied as a Planckian radiation source boundary condition in our calculations. For each experiment, two channels of VISAR data were acquired, corresponding to two different thicknesses of the stepped payload. The depth of 154 μm corresponds to VISAR A, or Z189A and Z190A and the depth of 308 μm corresponds to VISAR B, or Z189B and Z190B. These two thicknesses are equivalent to differing propagation distances for the generated shock wave.

If the measured shock wave is steady, then the active shock breakout diagnostic measures shock speed and the VISAR diagnostic measures material speed simultaneously. Together, these quantities determine the dynamic pressure and density of the sample, hence the equation of state, via the steady state Hugoniot relations:

Analysis of Z Pinch Shock Wave Experiments

$$\begin{aligned} P &= \rho_0 U_s u_p \\ \rho_0 U_s &= \rho(U_s - u_p) \end{aligned} \tag{1}$$

In Equation (1) the variables are: ρ_0 is initial density, ρ is the dynamic density, U_s is the shock speed, u_p is the material speed, and P is the pressure.

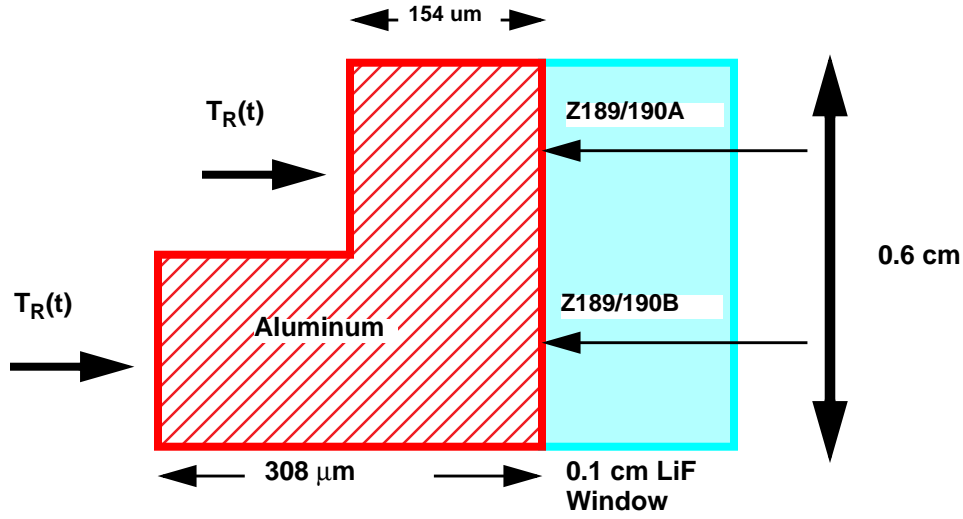


Figure 4. Schematic of payload for shots Z189 and Z190. The schematic is not to scale. The payload is not axisymmetric with respect to the axis of the secondary hohlraum. Viewed axially, its cross section is that of a 0.6 cm by 0.4 cm rectangle. The alignment is such that the sample depth for VISAR A is closest to the short side of the secondary hohlraum (Figure 2).

Drive Characterization

A full description of radiation drive diagnostics is provided in Reference 2. We will only summarize this information here. The primary diagnostic used on the Z machine for determining x-ray fluxes and equivalent Planckian radiation temperatures in hohlraums is a five-channel filtered time-resolved X-Ray Detector (XRD). This instrument measures x-ray flux over a photon energy range of roughly 100 eV to 2.3 keV. These data are then unfolded to provide an x-ray spectrum, peak x-ray power, and total x-ray energy. Time-resolved resistive bolometers also provide additional and complementary x-ray measurements. An illustration of the unfolding of a measured XRD spectrum and its fit by an “equivalent” Planckian distribution is given on page 2108 of Reference 2. For our purposes, it simply suffices to stress that the x-rays developed in the primary hohlraum are

Analysis of Z Pinch Shock Wave Experiments

expected to be thermalized, hence Planckian, and that the resulting Planckian time-dependent emission is unfolded from the XRD data.

The XRD can be used to measure Planckian radiation in the secondary hohlraums, via diagnostic apertures. The diagnostic aperture, as was fielded on Z189, is used to perform this measurement. On Z190, a similar diagnostic was fielded on the other identical secondary hohlraum which housed the fiber-optic shock breakout diagnostic. In this case, this drive history was assumed to be identical to what would have been measured directly in the secondary hohlraum used for the VISAR experiments.

Figure 5 shows the measured Planckian drive data for Shot Z189, along with a smoothing of the raw data. The smoothing was performed using ten point averaging on the raw data points. We performed this smoothing for computational purposes. High frequency oscillation in the computationally applied drive may create additional computational effort in our simulations. In undocumented previous work, we have confirmed that we can reproduce essentially the identical shock wave behavior by using the smoothed data, at somewhat less computational cost. Figure 6 shows the raw and smoothed Planckian data for Shot Z190. It is worth pointing out that the raw drive characterization for Shot Z189 is considerably noisier in the temperature regime near 30 eV and below. This may be due to an interaction between the smaller volume hohlraum and the diagnostic aperture, which is not present for the larger volume hohlraum of Z190. Given that the physical conditions of the Z-pinch source are identical for both experiments, the difference we see in peak temperatures between the Z189 and Z190 drives can be explained by the difference in volumes of the secondary hohlraums.

The drive timing in Figures 5 and 6 is in ALEGRA calculation time. The raw drive data were reported relative to the so-called Z machine *zero time*, which is the time when firing of the Z machine is initiated. Thus, a time shift in the raw data has been applied in these plots. We will have further occasion to discuss timing specifics below when we discuss our comparisons with the VISAR data measured on these experiments.

The drives shown in Figures 5 and 6 have not been corrected for the diagnostic aperture closing during the course of the measurement due to ablation from the radiation pulse, nor for the albedo of the gold emitting surface, which is less than (but close to) unity. Both of these effects tend to reduce the apparent measured Planckian peak drive temperature, by perhaps as much as 10 eV. In other words, the peak temperatures in Figures 5 and 6 may be low by as much as 10 eV. Also, we can not directly place error bars on these curves. In Reference 2, neglecting certain sources of error, a radiated energy measurement was believed to have an error of around 11%. Directly scaling this to a radiation temperature would lead to error bars around the Planckian temperature values of almost 50%. We are not claiming that the error bars are actually this large, but they could be.

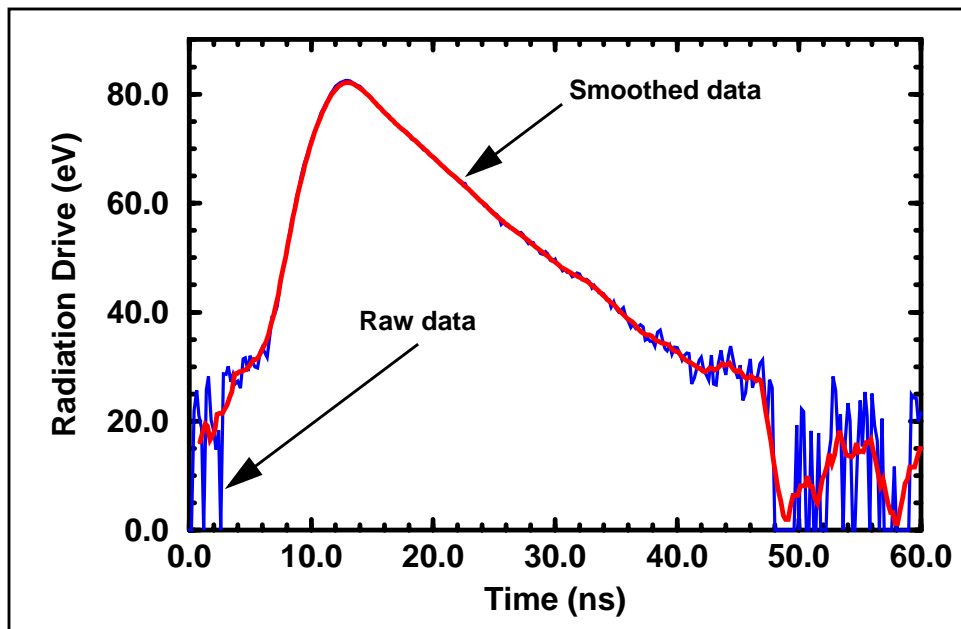


Figure 5. Smoothed drive overlaid with raw data for Z189

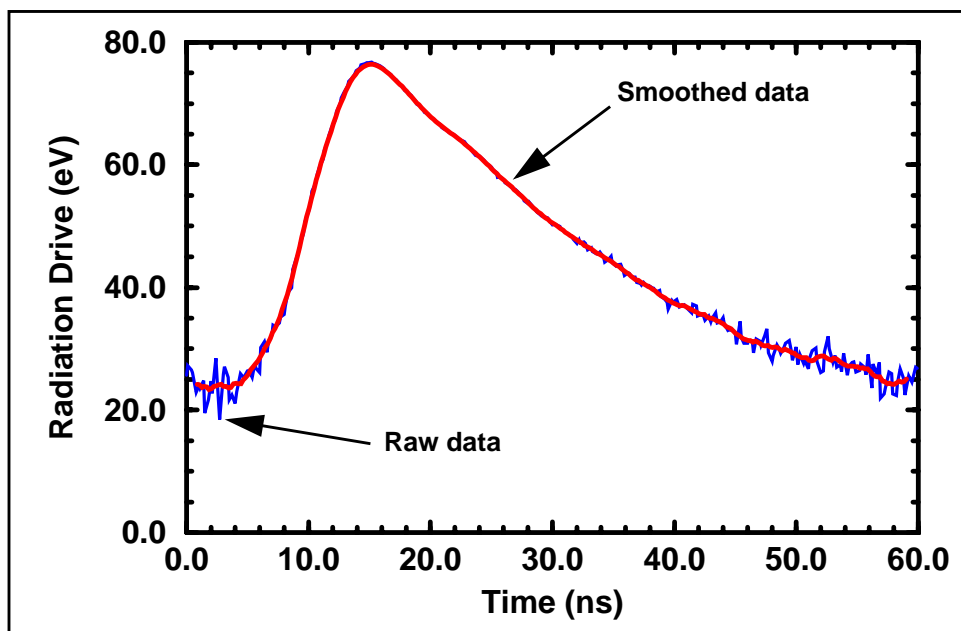


Figure 6. Smoothed drive overlaid with raw data for Z190

Analysis of Z Pinch Shock Wave Experiments

Finally, we comment that the radiation pulse experienced in a secondary hohlraum of the type described above would normally mimic the radiating characteristics of the Z-pinch itself. This creates a so-called “run-in” radiation pulse, having a duration of up to 80 or 90 ns, beginning at a very low temperature and extending to somewhere around 20 to 30 eV. Such a pulse is known to create precursor motion in experimental payloads well before the arrival of the main shock. In addition, there are significant diagnostic problems associated with applying the five-channel XRD diagnostic to measurement of the radiation drive below approximately 20 or 30 eV. Thus, the purpose of the Parylene burnthrough foils applied in these experiments is to remove this run-in pulse. Previous experience on the Z machine by a Los Alamos experimental team has shown that these burnthrough foils are effective at removing the run-in pulse [7], while still maintaining the peak drive temperature that would occur in the absence of a burnthrough foil.

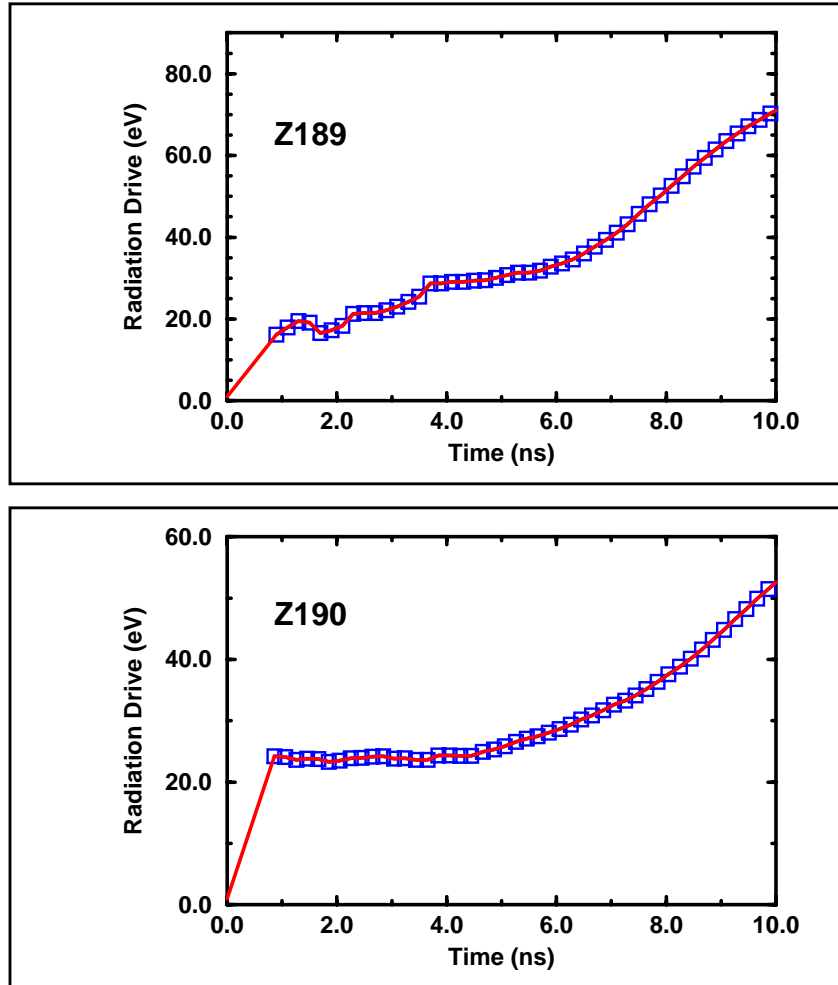


Figure 7. Extrapolated drive below 30 eV for Z189 and Z190. The boxes show the unextrapolated data, while the solid curve shows the linear extrapolation to $t=0.0$ ns, $T_R=1.0$ eV for times less than one nanosecond.

Analysis of Z Pinch Shock Wave Experiments

The smoothed drive has a lower threshold around 20 eV for Shot Z189, and around 22 eV for shot Z190, at the calculation zero time. For the analysis reported here we chose to start the drive at 1 eV, at time zero, for both experiments. This is compatible with the observed performance of the burnthrough foils, although there is intrinsic uncertainty in the XRD measurements below the two cutoff temperatures. The Los Alamos collaboration used a diagnostic (a silicon diode) that is more sensitive to lower temperatures in the drive, and observed that the truncation of the radiation drive was very close to our treatment here. The precise way we have modified the drives is shown in Figure 7, where the drives are plotted over the calculation time period of zero to ten nanoseconds. We discuss the sensitivity to this feature of our calculations later in this report.

Discussion of VISAR Data

The VISAR velocity interferometry system is a standard technique for diagnosing the time-resolved behavior of propagating shock waves [5-6]. As stated in the above discussion, there were two sets of VISAR data collected for each of the two experiments, one at a depth of 154 μm , the other at 308 μm for each experiment. The use of the lithium fluoride makes the measurements *in situ*, to a very good approximation, because the shock impedance of lithium fluoride is so close to that of aluminum.

The four data sets for these experiments are plotted in Figure 8. Our calculations predict that the corresponding generated pressures are between about 1 and 1.5 Mbars at these locations. The calculations also predict that the generated pressure wave has substantially attenuated and steepened during propagation to the experimental depths. This is not obviously seen in these data.

A careful analysis of the timing and particle velocity errors [4] in these data is summarized in the table below. Notice that the non-peak velocity errors are smaller than the symbols that we use to plot the data.

Table 1. Timing and particle velocity errors associated with Z189 and Z190.

Experiment	Timing Error (ns)	Peak Velocity Error (km/s)	Non-Peak Velocity Error (km/s)
Z189A	+5.2, -1.2	+0.3, -0.3	+0.04, -0.04
Z189B	+3.1, -5.1	+1.0, -1.0	+0.15, -0.15
Z190A	+1.6, -1.6	+0.3, -0.3	+0.04, -0.04
Z190B	+3.4, -3.4	+2.5, -0.0	+0.15, -0.15

Analysis of Z Pinch Shock Wave Experiments

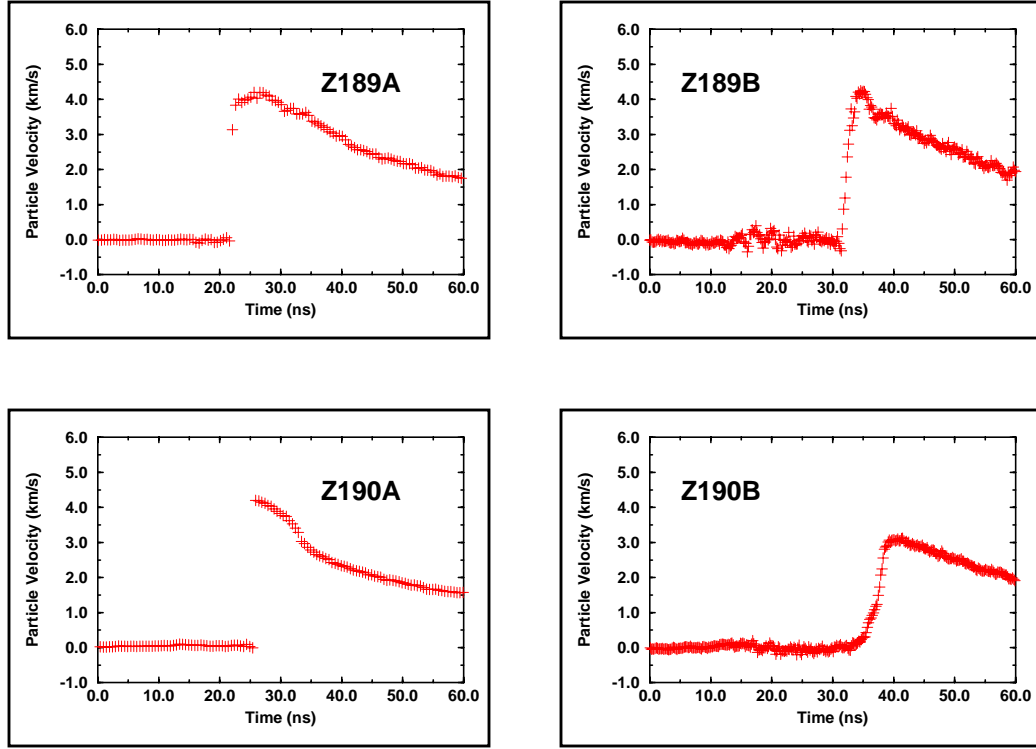


Figure 8. Visar data for Z189 and Z190

3. Calculations

Description of ALEGRA

A brief summary of ALEGRA can be found in Reference 3. As discussed there, ALEGRA is a multi-material, arbitrary-Lagrangian-Eulerian (ALE) strong shock wave physics code under development at Sandia National Laboratories. It combines the features of modern Eulerian shock wave physics codes with modern finite element Lagrangian codes. In ALEGRA, ALE shock hydrodynamics is finite element based. In addition to the basic shock wave physics hydrodynamics algorithms, a variety of coupled physics capabilities have been implemented, including coupled electro-mechanical response, magnetohydrodynamics, and radiation transport. Successful application of the code requires more than accurate implementation of solution algorithms for these types of physics. A variety of accurate material models (e.g. equation of state (EOS), constitutive and fracture, thermal conduction, radiative opacity, electrical resistivity, piezoelectric and ferroelectric material descriptions) must also be implemented. The specific material models used in our calculations of Z189 and Z190 will be discussed below.

ALEGRA is written predominantly in the C++ programming language to take advantage of object-oriented programming (OOP) techniques, although we have limited our use of

Analysis of Z Pinch Shock Wave Experiments

some features of C++ to avoid efficiency problems. We have also recognized the utility of incorporating various Fortran-based models and libraries if they best serve our modeling needs and if they are sufficiently mature and robust. In many cases there is little advantage to rewriting such software, even if resources were available to do this. Examples include the SESAME EOS interface, as well as the XSN in-line analytic opacity package that we use.

While the basic development of ALEGRA is performed on a variety of serial workstations, the code has also been designed to run on several distributed-memory parallel computers, especially ASCI (Accelerated Strategic Computing Initiative) class computers. All of the calculations discussed in this report have been run serially on Sun workstations, partly because the SPARTAN radiation package has not been implemented for parallel computers.

The present calculations are performed with strictly Lagrangian radiation-hydrodynamics. Aluminum is the only material modeled in the calculations. Lithium fluoride is not included directly as a distinct EOS. Instead, aluminum is also used as a surrogate for this compound, a good approximation given the very close shock impedances of the two materials over the range of pressures developed in Z189 and Z190. A full-range tabular SESAME EOS, #3715, is used to describe the aluminum. This table originates with the Los Alamos National Laboratory Theoretical Division EOS group [8]. No material strength is included in the calculations reported here. The yield strength of 1100 aluminum is on the order of 1 kbar, a number which is completely overdriven by the megabar-level pressures developed in the shocks formed for experiments Z189 and Z190.

Description of SPARTAN

The radiation transport package applied in the present modeling is the SPARTAN package (version 2.7). SPARTAN is an implementation of a simplified P_N radiation transport algorithm. It is denoted SP_N for short.

The fundamental equation to be solved in radiation transport is the *equation of transfer*, given in equation (2) below.

$$\frac{1}{c} \frac{\partial I}{\partial t} + n_i \frac{\partial I}{\partial x_i} = \kappa B + \sigma J - \chi I \quad (2)$$

In this equation, I is the specific radiative intensity as a function of seven variables - three spatial coordinates (x_i), time t , two angular coordinates (\hat{n}_i) (a unit vector), and energy frequency ν . B is the Planck function, κ is absorption opacity, J is the mean intensity (the zeroth moment with respect to angle of the intensity), σ is the scattering opacity, and χ is the total opacity. In radiation-hydrodynamics problems, the opacities are functions of material density and temperature., as well as radiation energy (or frequency).

Analysis of Z Pinch Shock Wave Experiments

The major difficulty with the full equation of transfer is that it is an integro-differential equation for radiative intensity as a function of the seven independent variables. When coupled to moving material in three space dimensions (radiation-hydrodynamics), the conservation laws of continuum physics must be solved in addition to the radiative transfer equation. However, the computational work associated with solving these equations is considered to be too great for practical applications at the present time. Hence, approximate schemes for treating the transfer equation are always used.

The most widely used approximate radiation transport method applied in radiation-hydrodynamics calculations is the multi-group diffusion method, which is described in detail by Bowers and Wilson [9]. In this approximation, the angular dependence of the full transfer equation is removed completely. It also can be cast as resulting from taking the following limits simultaneously in (2):

$$\begin{aligned}\kappa &\rightarrow \infty \\ c &\rightarrow \infty \\ C_V &\rightarrow 0 \\ Q &\rightarrow 0\end{aligned}\tag{3}$$

(C_V is material constant volume heat capacity, while Q is a non-radiative thermal source term. Both of these quantities appear in matter conservation laws that we have elected not to display in this discussion.) The resulting asymptotic limit to low order yields the “non-equilibrium” diffusion approximation:

$$\begin{aligned}\frac{1}{c} \frac{\partial J_g}{\partial t} + \frac{\partial F_{g,i}}{\partial x_i} &= \kappa_g (B_g - J_g) \\ F_i &= -\frac{1}{3\kappa} \frac{\partial J}{\partial x_i}\end{aligned}\tag{4}$$

where we have introduced the index g to indicate a finite discretization of the energy variable. Thus, (4) is a system of equations, which must additionally still be coupled to the moving matter field.

Problems primarily arise with the application of this method to regions of low opacity, where streaming of radiation is most important. In fact, the diffusion approximation violates causality as well as physical diffraction characteristics of radiation beams. This leads to a hierarchy of corrections to diffusion, including flux-limiting. A recent article that surveys the need for correction of the diffusion approximation is Reference 10.

In contrast, a very accurate, but computationally less feasible, approach to calculating radiation transport in radiation-hydrodynamics problems is the P_N method [11]. With this method, the transport equation is directly solved using full angular discretizations based on Legendre expansion techniques. It is currently mainly applied in 1-D radiation-

hydrodynamic problems. We provide the P_1 equations, to contrast with the diffusion approximation (4):

$$\begin{aligned}\frac{1}{c} \frac{\partial J}{\partial t} + \frac{\partial F_i}{\partial x_i} &= \kappa(B - J) \\ \frac{1}{c} \frac{\partial F_i}{\partial t} + \frac{1}{3} \frac{\partial J}{\partial x_i} &= -\chi F_i\end{aligned}\tag{5}$$

which equations also result from the assumption that $I = J + 3n_i F_i$, called the Eddington approximation.

SP_N is an asymptotic treatment of the equation of transfer [12, 13]. SP_N is a generalization of the 1-D P_N equations to multiple dimensions in a simplistic manner that is not entirely accurate (if the generalization were done consistently, the more complicated P_N equations would be derived). Because of this, the SP_N solutions can not be expected to converge in the limit as the order $N \rightarrow \infty$, although they are exact for certain situations in this limit. However, they propagate information at finite speeds, limiting to the speed of light from below as the order increases. Thus, they are in theory more accurate than multi-group diffusion in low opacity regions. In fact, SP_1 and P_1 are identical, while SP_N and P_N are identical for all N in 1-D slab geometries. The general form of the SP_N equations is:

$$\begin{aligned}\frac{1}{c} \frac{\partial \xi_n}{\partial t} + \frac{\partial \Gamma_{n,i}}{\partial x_i} &= \kappa(B - J) \\ \frac{1}{c} \frac{\partial \Gamma_{n,i}}{\partial t} + \mu_n^2 \frac{\partial \xi_n}{\partial x_i} &= -\chi \Gamma_{n,i} \\ J &= \sum_{n=1}^N w_n \xi_n\end{aligned}\tag{6}$$

It is convenient to regard ξ_n as a pseudo-intensity, through which the “true” mean intensity is recovered in the expansion (6) (third equation), and $\Gamma_{n,i}$ is a pseudo-flux. The w_n are expansion weights, while the coefficients μ_n are the exact Legendre expansion coefficients that would appear in the P_N expansion for a 1-D geometry. The efficient numerical solution of the equations (6) still relies upon solution of diffusion equations. The SPARTAN package [14, 15, 16] that implements this method, linked in ALEGRA, was written by M. L. Hall of Los Alamos National Laboratory. SPARTAN uses *diffusion synthetic acceleration* (DSA) [17]. DSA is a means of providing a transport solution more rapidly, basically by using a diffusion solution to accelerate a transport solution. SPARTAN also uses an additional transport solution acceleration technique, called Linear Multi-Frequency

Grey Acceleration. In the present work, we strictly use SP_1 for our baseline calculations, although we will compare with SP_3 and SP_5 below.

The XSN opacity model [18] is used to calculate the needed opacities in ALEGRA. Minimal information is required to apply this scheme in the present application, namely the atomic number (13) and atomic mass (26.98154 amu) of aluminum.

Calculation Set-Up Information

A one-dimensional projection of the basic hydrodynamic computational algorithms in ALEGRA has not been implemented. Hence, we mesh our “one-dimensional” simulations of the Z189 and Z190 experiments as shown in Figure 9, in a single line of two-dimensional finite elements having boundary conditions appropriate for calculating one-dimensional uniaxial strain.

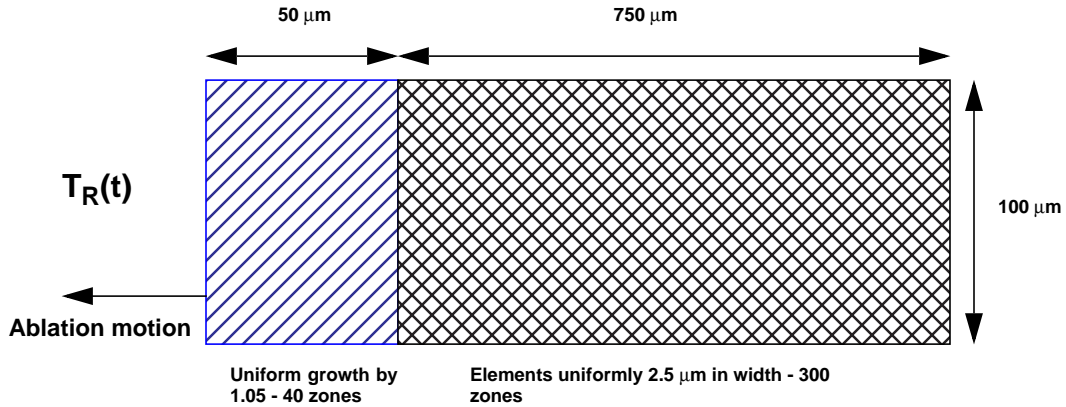


Figure 9. Definition of meshing in the aluminum used in our calculations (not to scale).

The mesh is divided into two regions. In the first, containing 40 elements, a variable mesh is used that starts with a very fine element of width approximately $0.4\ \mu\text{m}$ at the boundary where the Planckian radiation boundary condition is applied. The mesh grows geometrically by a factor of 1.05 over a distance of $50\ \mu\text{m}$. This is followed by a region of $750\ \mu\text{m}$ in which 300 elements of $2.5\ \mu\text{m}$ width are used. The complete mesh thus contains a sum of 340 elements.

Symmetry boundary conditions are applied to the top and bottom of the mesh, for both radiation transport and hydrodynamic motion. The hydrodynamic constraint enforces effectively 1-D uniaxial motion. The boundary condition at $800\ \mu\text{m}$ is hydrodynamically unconstrained, and a vacuum radiation transport boundary is applied. The boundary at $0.0\ \mu\text{m}$ is also hydrodynamically unconstrained, while it is radiatively specified by a time-dependent Planckian source. This source is defined as in Figures 5 through 7. The mesh was

generated by a Sandia mesh generation code, FASTQ [19]. Complete specification of the needed inputs for both Z189 and Z190 are given in Appendix B.

Analysis of Shot Z189

Ablation shocks are generated by the reaction (conservation of momentum) of cold material to the heating, vaporization, and expansion at high-velocities of aluminum that has absorbed drive radiation. Figure 10 shows some of the details of the expansion of ablated material in our simulation of Z189. The exposed surface expands at speeds near 150 km/s. This velocity rapidly decreases with increasing depth in the payload. The second part of the figure shows greater detail near the limiting depth of ablated material, which is around 18.4 μm . At this depth, there is no outward motion of material for the duration of the calculation. We will refer to this as the calculated *ablation depth*, and this seems to be a reasonable definition.

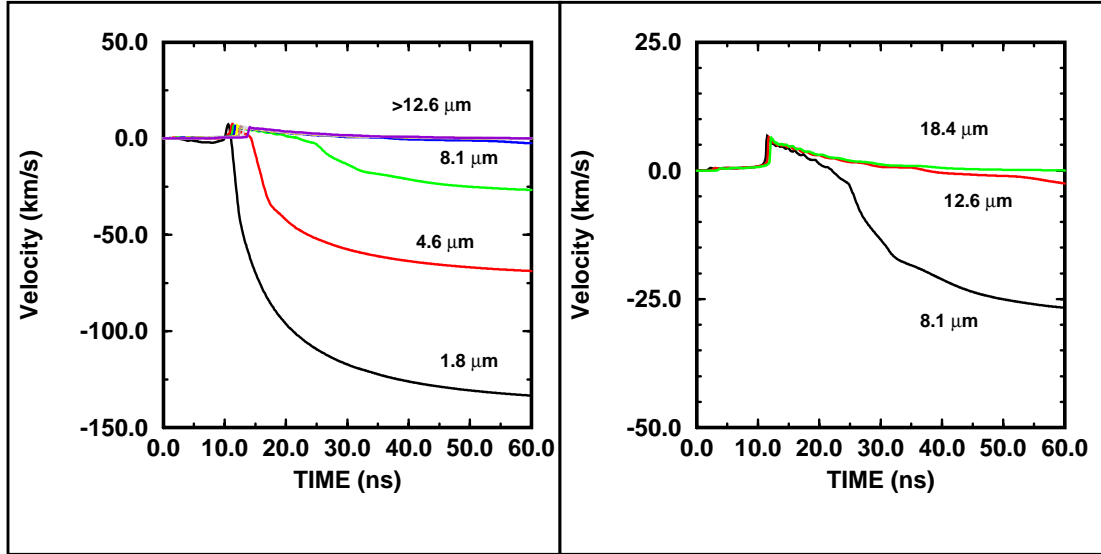


Figure 10. Ablation velocities of selected mass elements for Z189.

The resulting shock trajectory is shown in the t - x diagram in Figure 11. The first mass trajectory shown corresponds to the calculated ablation depth, 18.4 μm . At this depth, the influence of the early temperature gradient in the drive is apparent in the initial movement of that mass prior to the arrival of the shock. In addition, for depths less than 80 μm we note that the shock arrives prior to the peak of the drive. For depths greater than 80 μm , the shock is increasingly detached from the temporal gradient and peak value of the drive. Notice that the shock trajectory itself is curved, having smaller slopes at longer times. This reflects the lower shock velocities that apply as the peak amplitude attenuates.

For EOS experiments, we are always interested in whether preheat of the sample from the radiation drive itself takes place. This can corrupt EOS measurements, and complicate their analysis. Figures 12 and 13 examine the propagation of the radiation into the payload.

Analysis of Z Pinch Shock Wave Experiments

Figure 12 shows the temporal behavior of the radiation temperature at payload depths of 18.4, 50, 154, and 308 μm , the latter two being the depths at which the VISAR records are acquired. For the two shallow depths, peaks of respectively 8 and 2 eV are apparent at approximately 13 ns, the time of peak drive. We predict no such feature at the experimental depths. Figure 13 shows that the radiation wave has not propagated to any depth close to the experimental locations by the time of peak drive. Finally, we note that the t-x diagram shows no material response at all at the experimental depths prior to the arrival of the shock, well beyond the time of the peak in the drive. The small bump in radiation temperature appearing at all locations near 1 ns calculation time is of unknown origin. We do not know if it is significant.

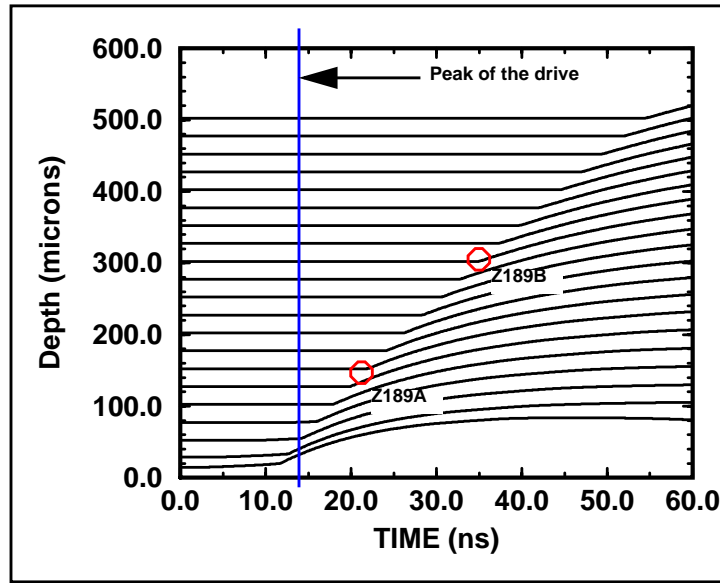


Figure 11. A t-x diagram for Z189. Motion prior to the arrival of the main shock appears to a depth of around 100 microns. Each curve shows the trajectory of the material element at the specified depth. The VISAR data collection depths are shown.

Specific details illustrating the nature of the shock wave propagation and attenuation for Z189 as predicted by ALEGRA are illustrated in Figure 14. We see that the shock pressure attenuation is approximately 0.6 Mbar by the time it reached 300 μm , or roughly 33% of its value at 100 μm . The ablation pressure at shallower depths is much greater, the largest value appearing in the baseline calculation being 2.6 Mbars, at the depth of approximately 15 μm , which is well within the ablated material. Significant shock attenuation has taken place by the time the wave passes through the experimental locations. We explicitly isolate our predictions for the shock pressures at the experimental locations in Figure 15. For Z189A, we predict the shock pressure to be 1.6 Mbar, while for Z189B we predict it to be 1.2 Mbar.

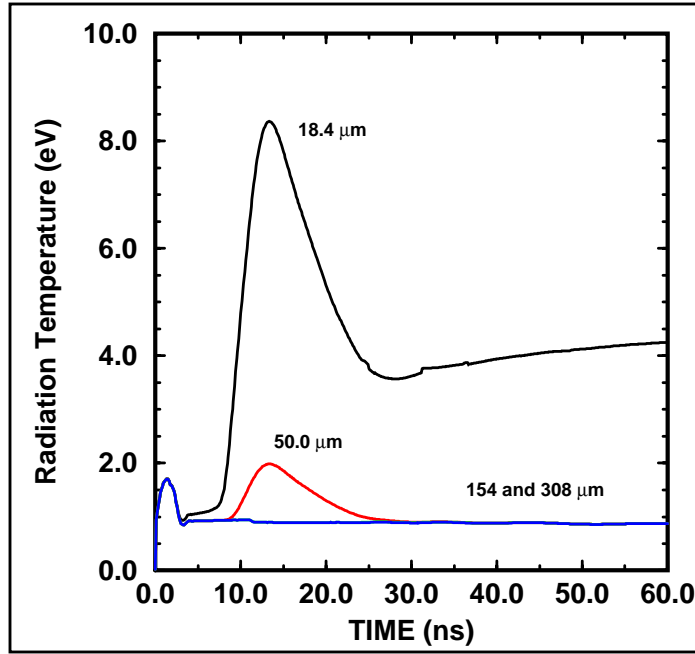


Figure 12. Radiation temperature histories at 18.4, 50, 154, and 308 μm .

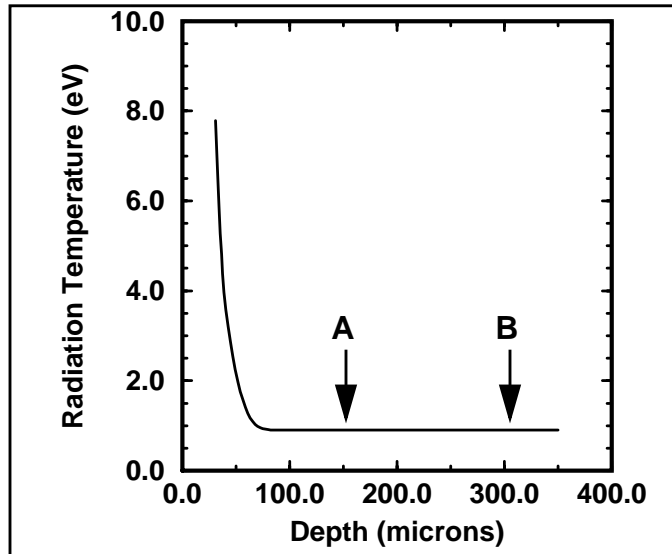


Figure 13. Radiation temperature vs depth at peak drive time of 13.0 ns, where A and B indicate the positions at which the experimental velocity records were taken.

Analysis of Z Pinch Shock Wave Experiments

We have shown the equivalent information for particle velocities in Figures 16 and 17. The particle velocity attenuates by 19% over the same range of depths as we discussed for the shock pressures, 100 to 300 μm , in Figure 16. Figure 17 isolates the predicted particle velocity histories at the measurement depths. The overlays of these predictions with the actual experimental VISAR data are shown in Figures 18 and 19. The error bars reported in Table 1 are also shown in these plots.

We need to specifically mention a timing issue that has been incorporated within the calculation-VISAR data overlays. For purposes of our calculations, we established the calculation zero time to be the beginning of the drive data used in each calculation. This time corresponded to 2520 ns for both Z189 and Z190. The VISAR data used a timing zero that corresponded to so-called peak pinch time. This is 2532.8 ns for Z189, and 2535.9 ns for Z190. Thus, to properly locate the experimental data in the timing frame of our calculations, the VISAR data for Z189 must be shifted by $(2532.8 - 2520)$ ns, or 12.8 ns. That for Z190 must be shifted by $(2535.9 - 2520)$ ns, or 15.9 ns.

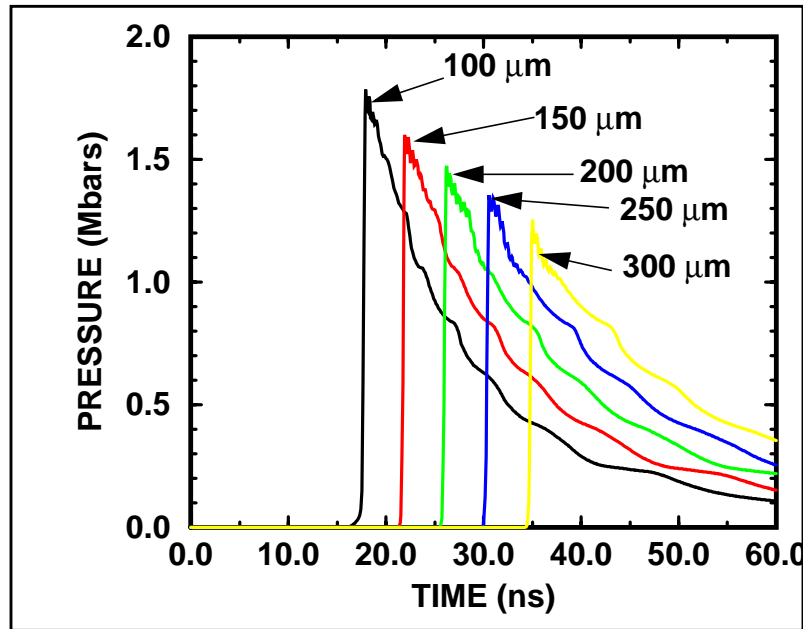


Figure 14. Time histories of pressure as a function of initial depth in the sample.

Analysis of Z Pinch Shock Wave Experiments

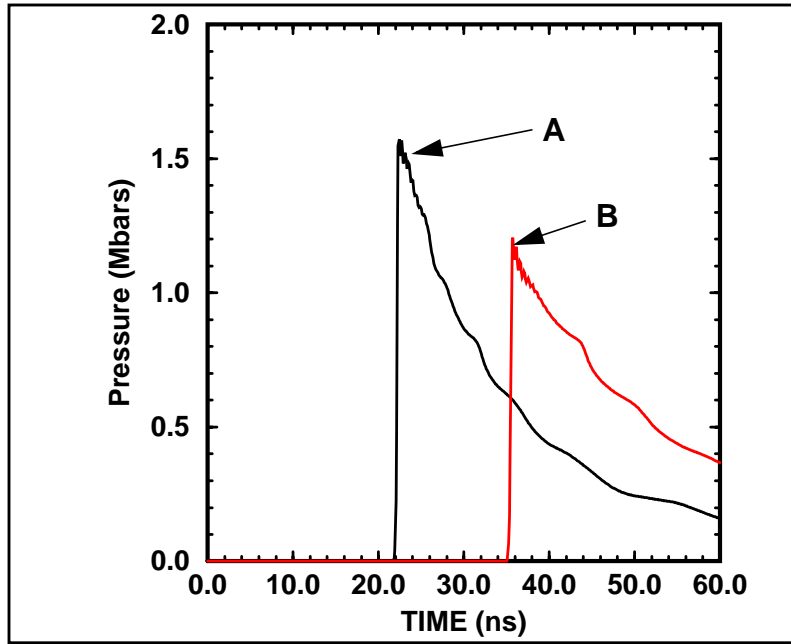


Figure 15. Pressures at diagnostic locations for Z189A and Z189B.

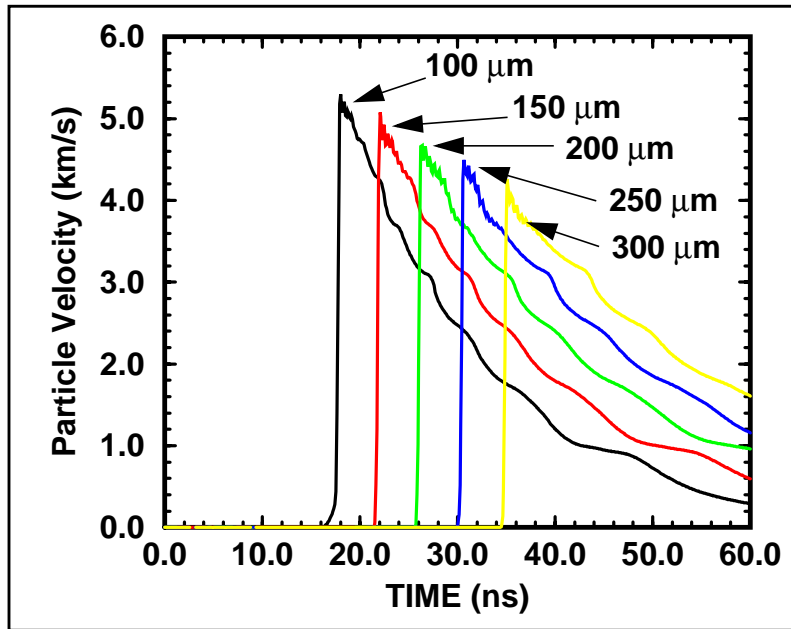


Figure 16. Particle velocity attenuation as a function of initial depth in the sample.

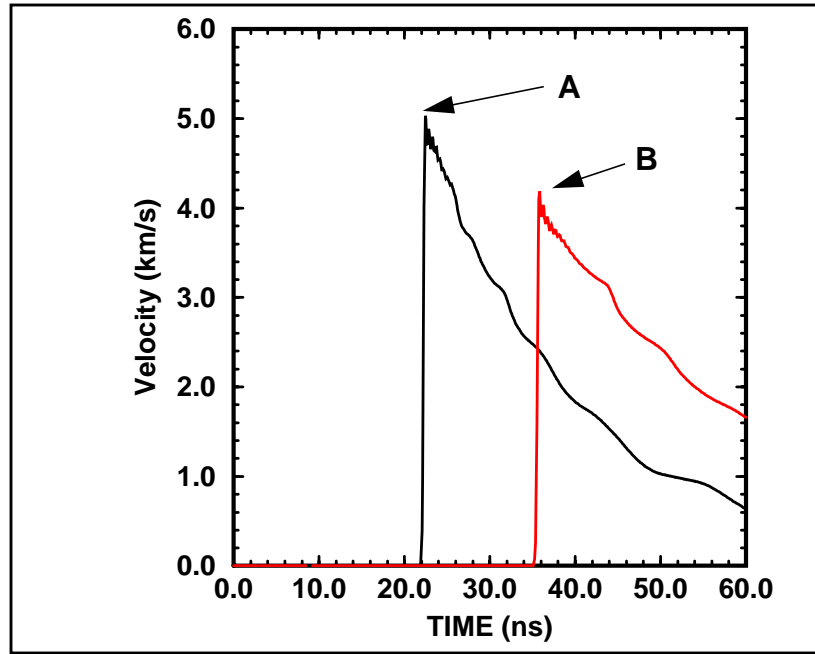


Figure 17. Computed particle velocity histories at the A and B locations for Z189.

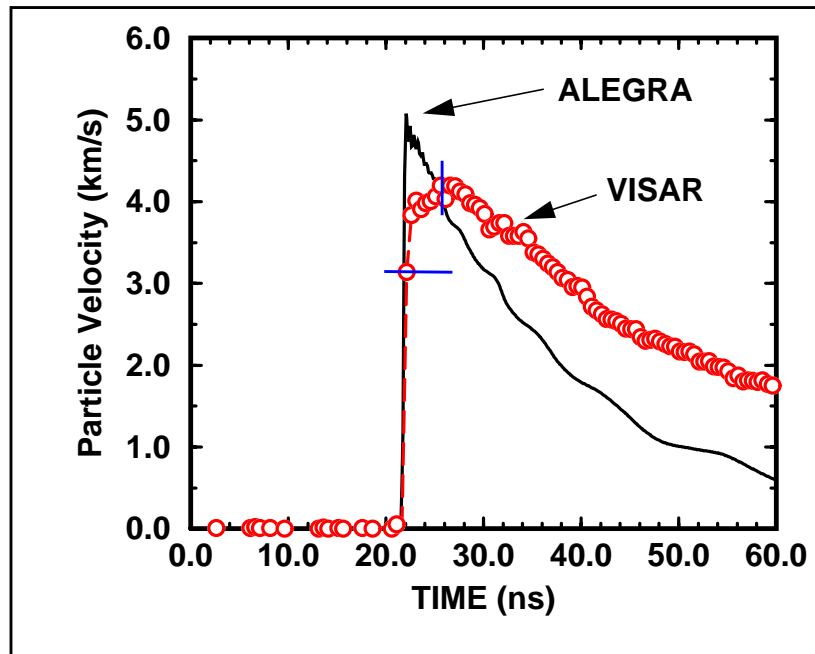


Figure 18. Comparison of computed and measured particle velocity histories at Z189A. The particle velocity non-peak error bars are smaller than the size of the symbols used for the experimental data.

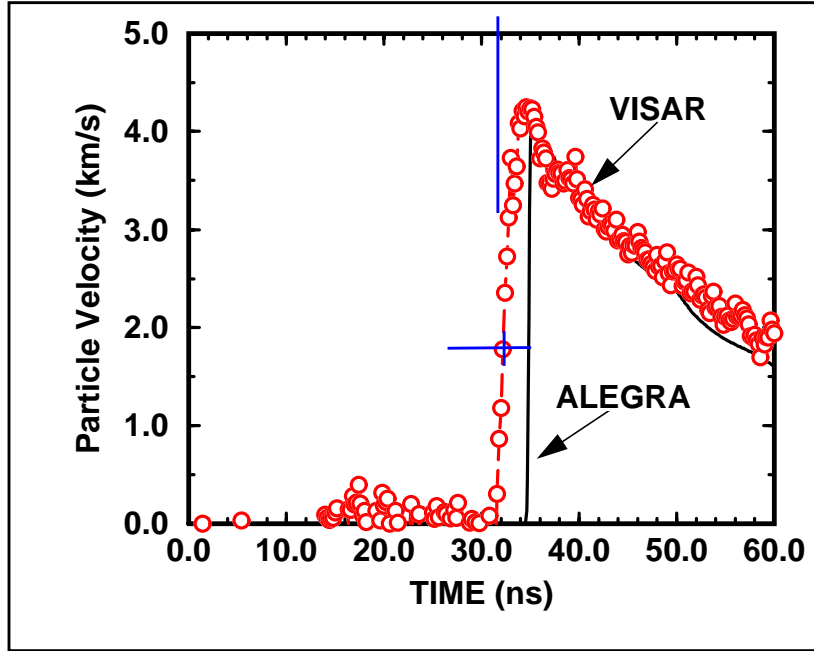


Figure 19. Comparison of computed and measured particle velocity histories at Z189B.

Analysis of Shot Z190

Z190 should be viewed as a Z-pinch source repeat of shot Z189. The only computational difference is the radiation temperature drive. Therefore, ablation details, radiation penetration and the shock behavior should be quantitatively similar. This is, in fact, the case, as shown in Figures 20 through 25. Since the apparent measured peak drive temperature is somewhat smaller for Z190, our calculated shock amplitudes are also smaller. However, we stress again that we predict that there is no drive prepulse induced motion or radiation preheat at the experimental locations. The corresponding particle velocity attenuation associated with the propagating shock wave is plotted in Figure 26.

The small blip seen in Figure 12 near 1 ns is also present in Figure 22, but slightly different. It remains unclear what the origin of this feature is. It may be due to our rapid initialization of the drive data from 1 eV, or it may be an artifact due to unknown errors in the calculations.

Analysis of Z Pinch Shock Wave Experiments

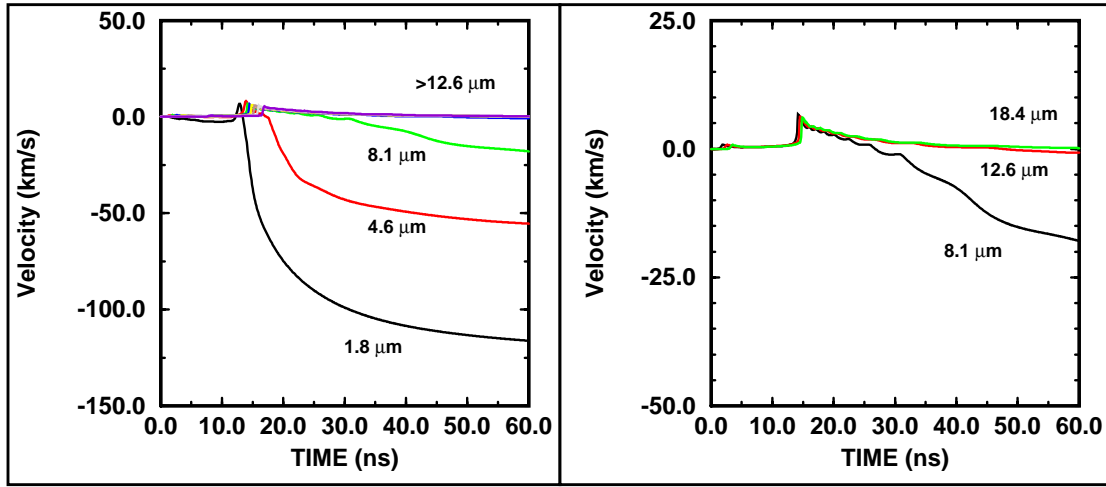


Figure 20. Ablation velocity for Z190.

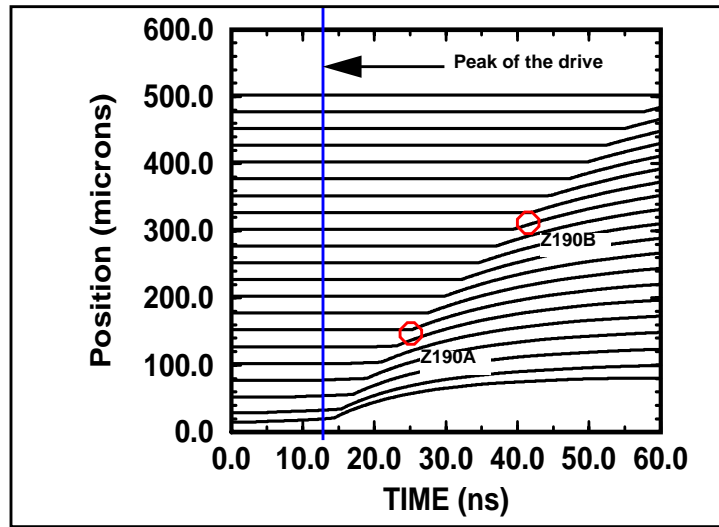


Figure 21. An x-t diagram for Z190. Motion prior to the arrival of the main shock appears to a depth of around 100 microns.

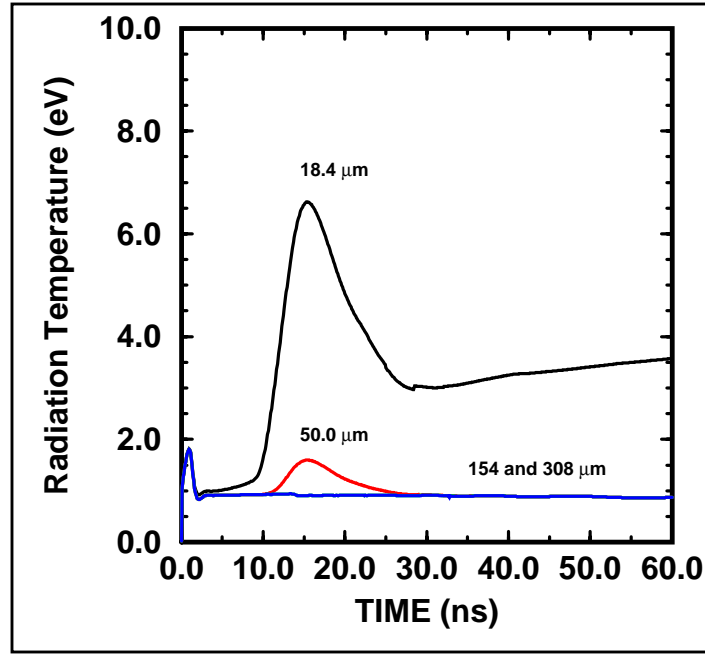


Figure 22. Radiation temperature histories 18.4, 50, 154, and 308 μm .

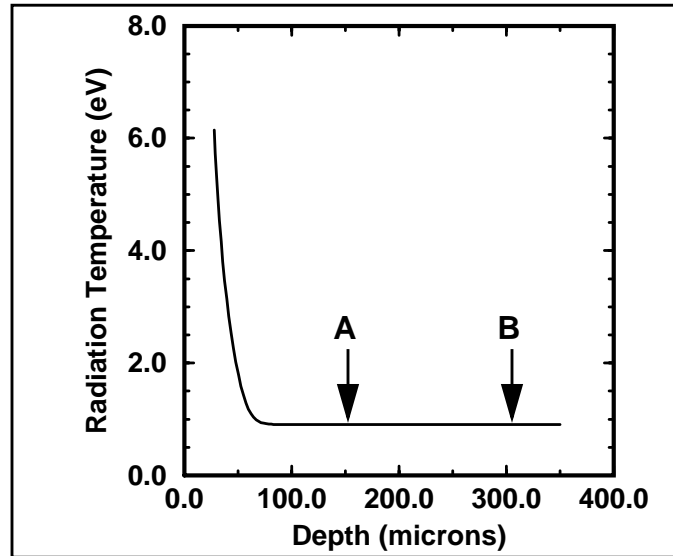


Figure 23. Radiation temperature vs depth at peak drive time of 15.0 ns, where A and B indicate the positions at which the experimental velocity records were taken.

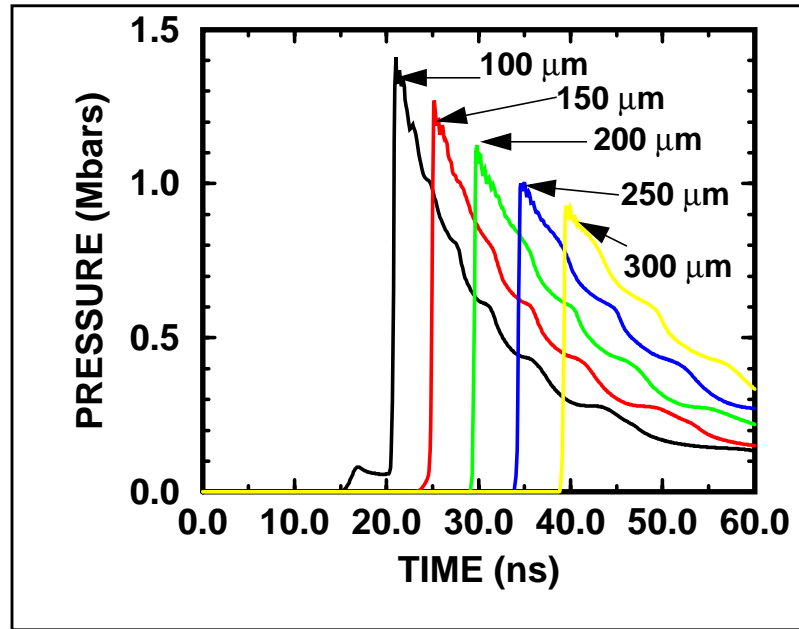


Figure 24. Time histories of pressure as a function of initial depth in the sample.

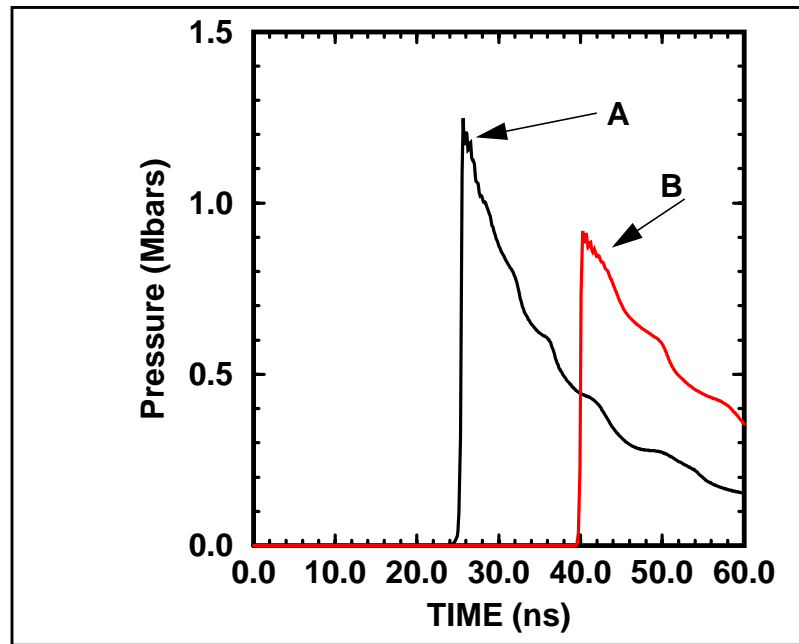


Figure 25. Pressures at diagnostic locations for Z189A and Z189B.

Analysis of Z Pinch Shock Wave Experiments

The most interesting difference between Z189 and Z190 when examining the pressure propagation is that a small “foot” is still apparent in the Z190 shock wave (and particle velocity as well) at 100 μm . This effect is seen in the Z189 analysis at shallower depths. Therefore, there are sufficient differences between the drives for these experiments to make this feature persist at greater depth for Z190. Figure 27 shows that the shock has finally overdriven the foot by the time it propagates to the Z190A experimental location, except for a very slight rounding at the base of the predicted shock wave.

That the shock is still slightly underdriven at the Z190A position is also predicted in our particle velocity record for that depth. The experimental VISAR data are overlaid with the calculation in Figures 28 and 29. Note that the experimental data for Z190A are inadequate to resolve whether the calculation prediction that the shock wave is slightly underdriven at that location is correct. This is because the timing errors are larger than the temporal width of the calculated feature. Although it was not the purpose of these experiments to provide such fine detail, this is the type of question that pertains to the use of VISAR measurements as supplemental drive diagnostics. Nonetheless, it is easy to believe, given various inaccuracies in our calculations, that the shock is actually fully developed by the time it propagates to the depth of 154 μm .

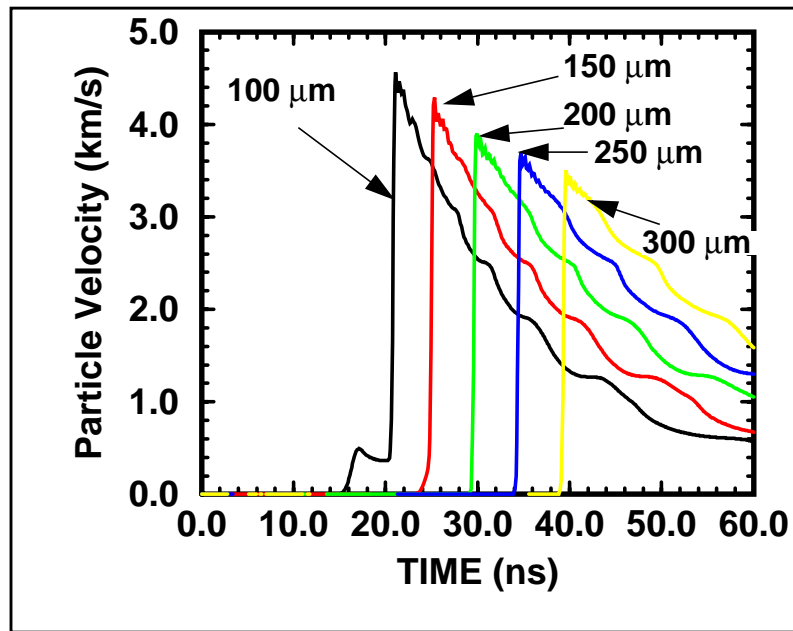


Figure 26. Particle velocity attenuation as a function of initial depth in the sample.

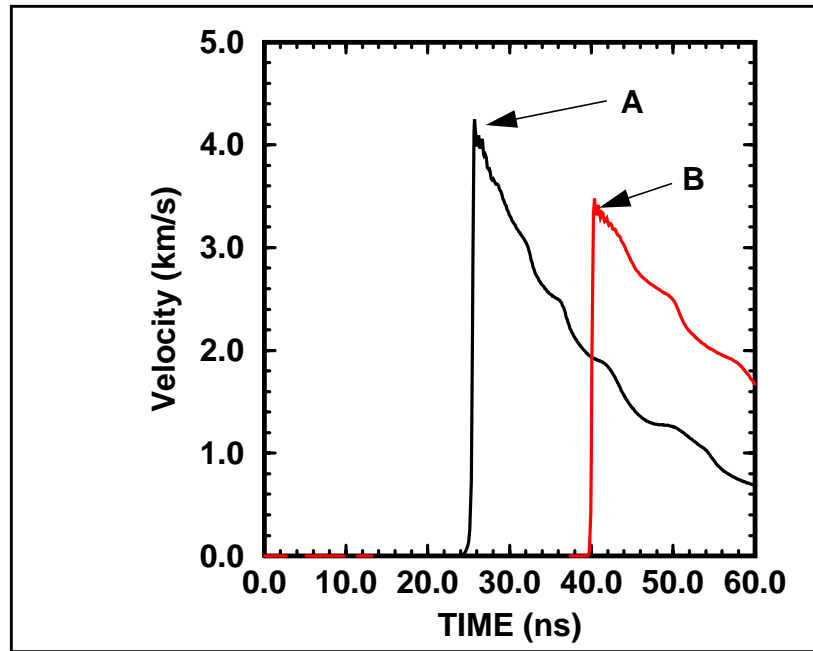


Figure 27. Computed particle velocity histories at the A and B locations for Z190.

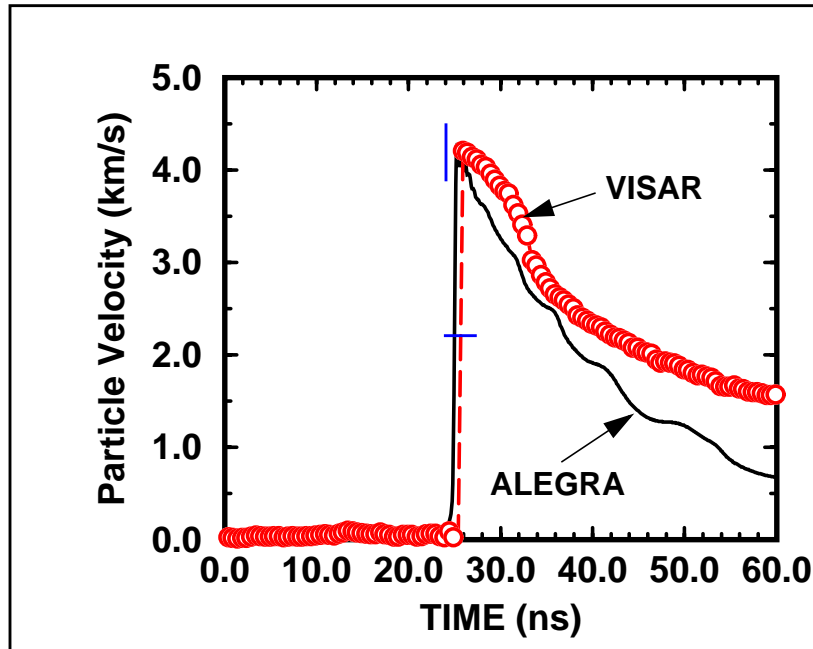


Figure 28. Comparison of computed and measured particle velocity histories at Z190A. The non-peak particle velocity error bars are smaller than the size of the symbols used for the experimental data.

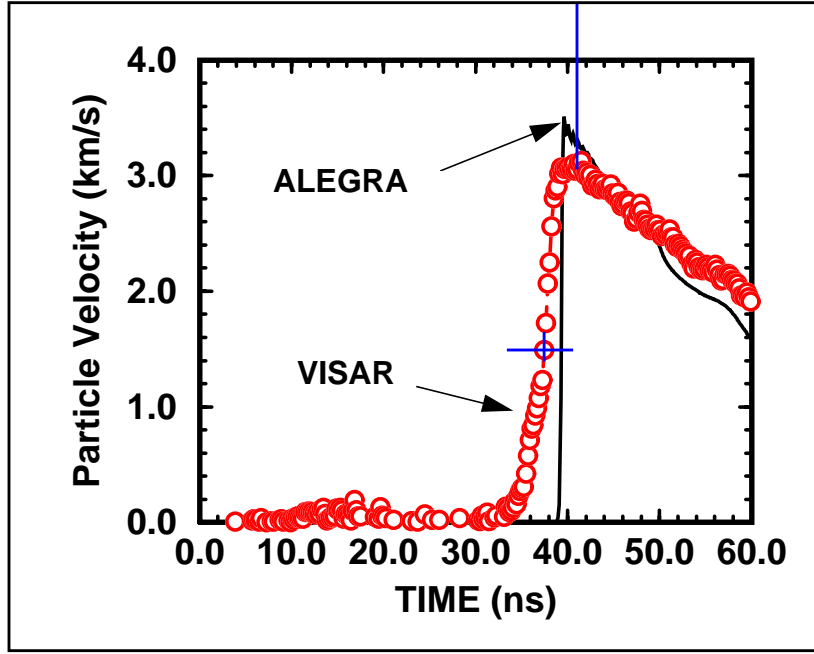


Figure 29. Comparison of computed and measured particle velocity histories at Z190B. The peak velocity error bar is off the scale of the plot.

The finite gradient seen in the experimental data for Z190B must give us pause. It can not be explained in terms of our computational analysis. If we accept the experimental data at face value, it demonstrates that the shock wave is actually becoming less steep as it propagates, which is not possible under normal conditions in a nonlinear material like aluminum. As discussed further below, what we are likely seeing in the Z190B data is a symptom of the irregularity of the drive in this experiment. What is interesting is that the irregularity seems more pronounced in Z190, when the large diagnostic aperture present in Z189 was missing. This would fully explain the seemingly contradictory nature of the data. We can only explore this issue computationally with 2-D simulations, something we do not pursue in this report.

Sensitivity Studies

Dependence on the number of groups:

The baseline calculations compared with the experimental data in Figures 18, 19, 28, and 29 resolved the radiation between 1 eV and 6 keV with 18 logarithmically distributed groups. We have studied the sensitivity of these calculations to the group resolution by performing a calculation in which we doubled to a total of 36 the number of groups in this energy range. We compare the particle velocity predictions at the experimental locations with those from the baseline calculation for experiment Z189 in Figures 30 and 31.

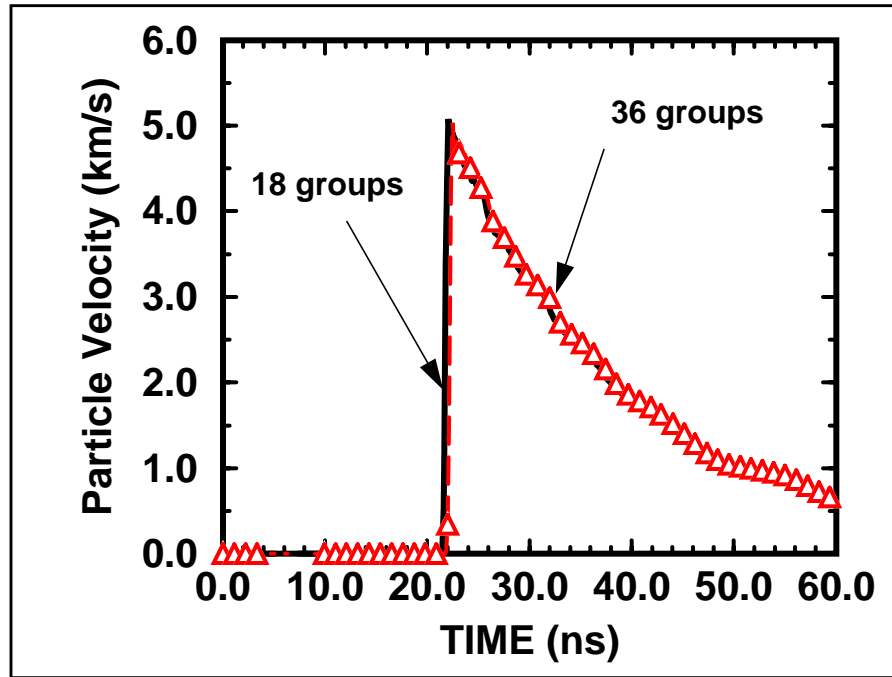


Figure 30. 18 versus 36 energy groups for Z189A. Triangles denote 36 groups.

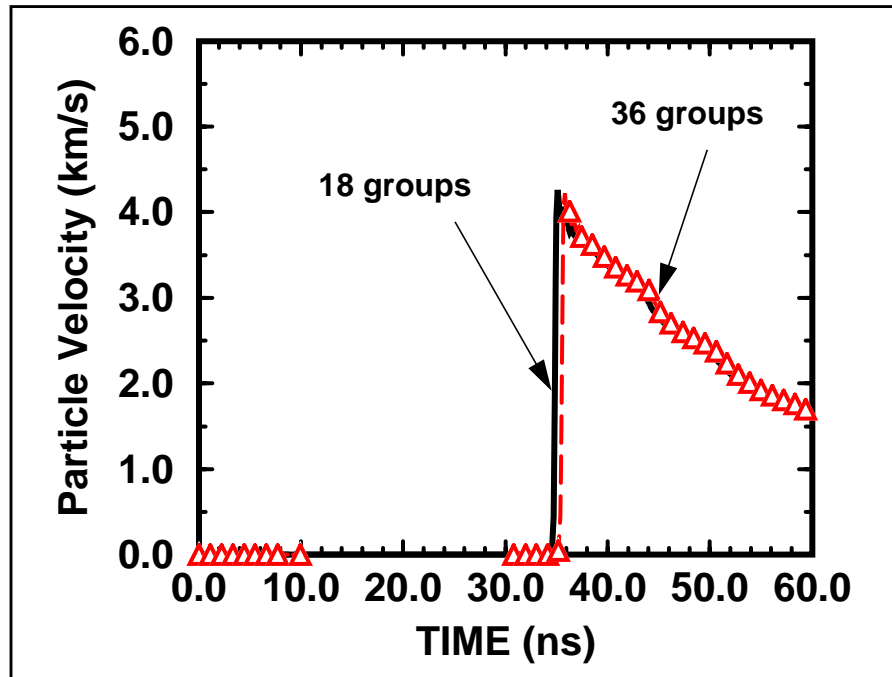


Figure 31. 18 versus 36 energy groups for Z189B. Triangles denote 36 groups.

The results are virtually identical for 36 groups as for 18 groups. There are larger differences between the two calculations in the ablation region. However, the key point here really is that these differences essentially disappear by the time and at the depths where the VISAR data is collected for particle velocity histories.

Sensitivity to the order of SP_N :

The SPARTAN SP_N package becomes more transport-like (in an asymptotic sense) for larger values of N . We ask whether this might significantly influence the details of the ablation, and possibly details of the particle velocity histories at the experimental locations, for the present simulations. We have assessed the influence of the SPARTAN order by performing calculations for Z189 with $N = 3$ and $N = 5$. The resulting predicted VISAR records are compared with the baseline calculation in Figures 32 and 33. These calculations were all performed with the nominal 18 group energy binning shown in Appendix B.

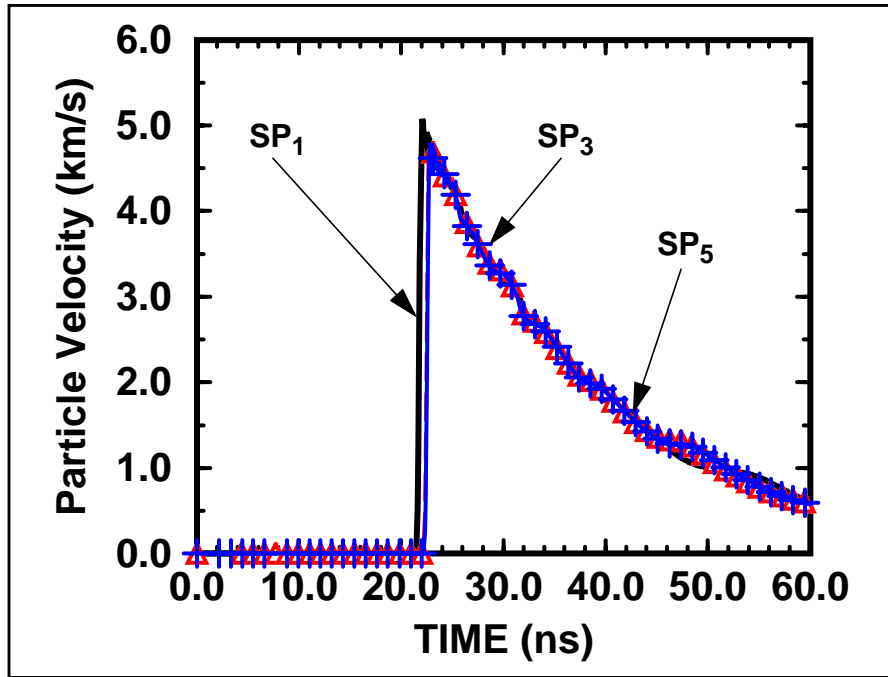


Figure 32. Comparison of SP_N calculations with $N = 1, 3, 5$ for Z189A. Triangles correspond to $N = 3$; crosses correspond to $N = 5$.

The most obvious thing to note about these comparisons is that there is a slight timing shift with respect to the baseline calculations. The wave at both locations is arriving later, corresponding perhaps to the slight decrease in amplitude of the wave. While the decrease in apparent shock amplitude is slightly more consistent with the experimental data shown in Figures 18 and 19, the increased time of arrival is not. The physics change with higher orders of SP_N seems to be reasonable though. The calculations suggest that slightly less net energy has been absorbed in the aluminum payload for $N = 3, 5$, resulting from a bit more radiative loss in the ablation plume. This slightly weakens the resulting ablation shock, resulting in exactly what we see in these comparisons.

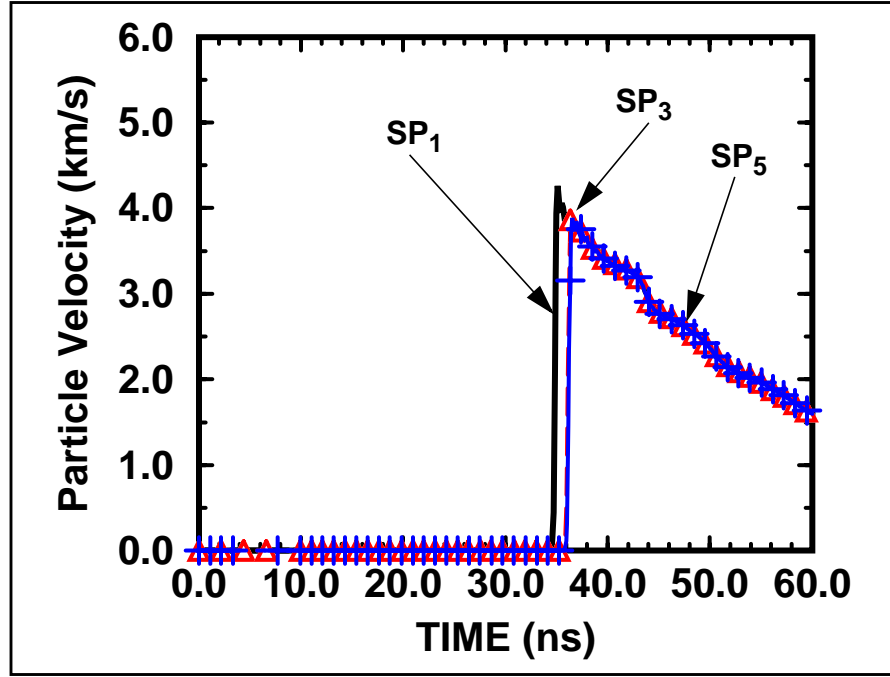


Figure 33. Comparison of SP_N calculations with $N = 1, 3, 5$ for Z189B. Triangles correspond to $N = 3$; crosses correspond to $N = 5$.

Sensitivity to the meshing used:

Simulation of the formation and propagation of ablative shocks by a radiation source is expected to be fairly sensitive to the meshing actually used in the calculation. For example, the fact that our baseline calculations do not match the convexity trends seen in the VISAR data at the A location might be due to lack of resolution in the ablation region.

To test the influence that this might have on our baseline comparison with the experimental data, we have performed a calculation in which the mesh spacing is smaller by between a factor of 0.2 to a factor of 0.5, depending on whether one looks at the region of varying mesh spacing or that of constant mesh spacing. We have compared the results with the baseline calculation for Z189 in Figures 34 and 35. the calculations look virtually identical. This suggests that our original meshing is well-converged for the baseline choices of SPARTAN order and group discretization. Thus, whatever is causing the differences in convexity between calculation and data in each experimental comparison is more than simply meshing resolution. For example, this could also be an artifact of drive heterogeneity across the face of the sample.

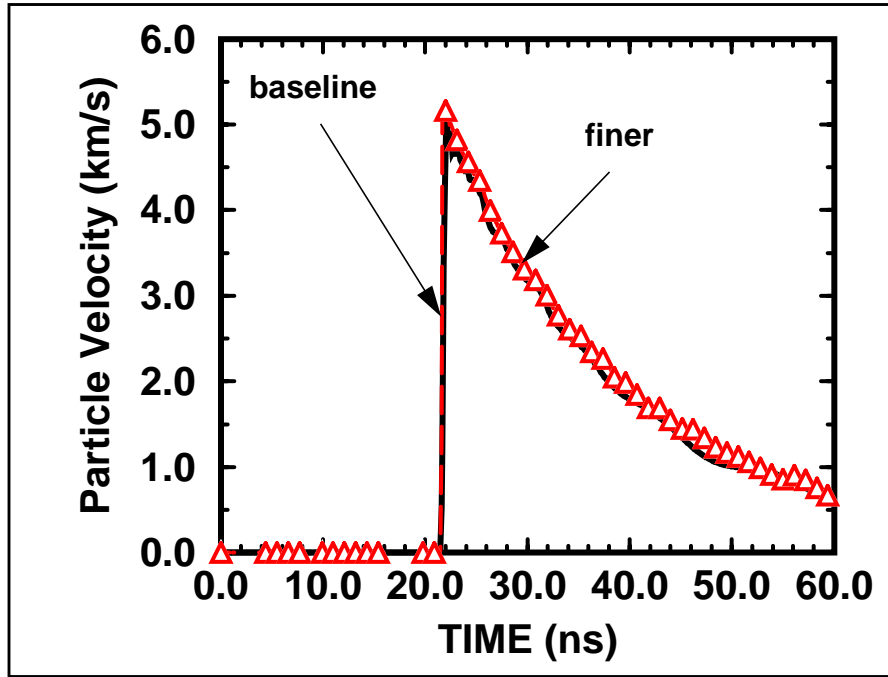


Figure 34. Baseline versus finer meshing for Z189A. Triangles are the finer meshed calculation.

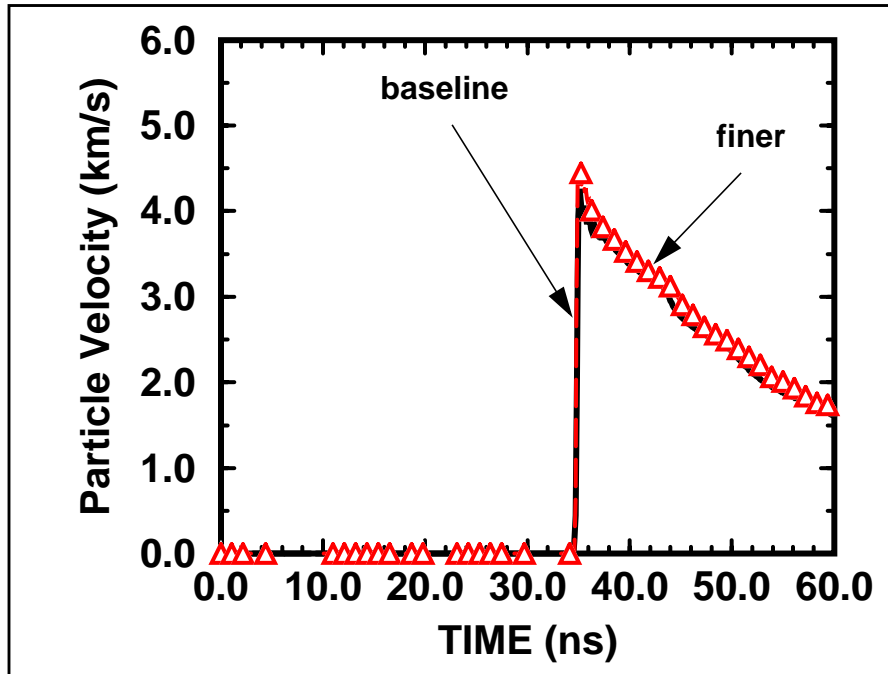


Figure 35. Baseline versus finer meshing for Z189B. Triangles are the finer meshed calculation.

Sensitivity to drive variation:

Another reason that there could be subtle differences in the shapes of the calculated VISAR records at location A compared to the experimental data could be inadequate representation of the true experimental radiative drive. There are many questions that arise when we consider how sensitive our calculations may be to variations in the radiative drive. Actually capturing the true variability of the drive, as measured by experimental error bars, as well as being able to resolve drive temperatures below the threshold of around 30 eV, is difficult to do for these experiments, as mentioned previously. Also, using systematic uncertainty analysis procedures for better determining the calculation sensitivity is not included in the scope of this paper. Thus, we will consider this issue with two representative comparisons.

First, we recall that Z189 and Z190 were intended to actually be repeat experiments. Therefore, the actual drive variation between these two shots could be considered to be some measure of the drive uncertainty. We have directly compared the calculated particle velocity histories at the A and B locations in Figures 36 and 37.

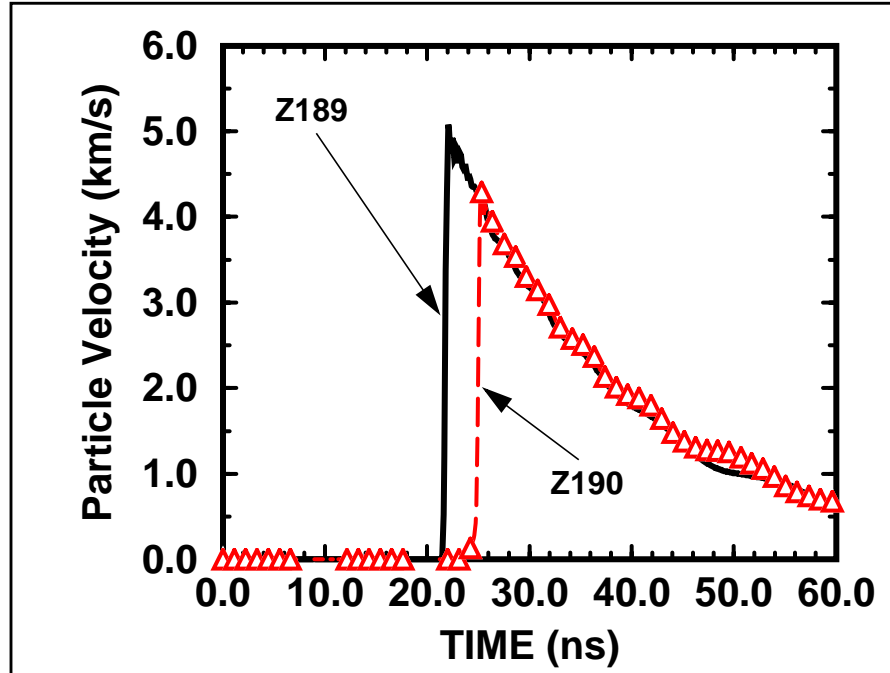


Figure 36. Z189A versus Z190A. Triangles are the ALEGRA calculation corresponding to Z190.

Because these are one-dimensional calculations, there is nothing that reflects the presence of diagnostic hole differences, or other things that could contribute to actual performance differences in the secondary hohlraums for the actual experiments. The differences between Z189 and Z190 seen are strictly due to perceived drive differences, which implicitly reflect a certain component of shot to shot variability as well as uncertainty in the measured drive. With this in mind, we simply stress that the observed differences are

quite large. Drive variability is definitely the most sensitive aspect of our calculations that we consider in this paper, as easily seen in these figures.

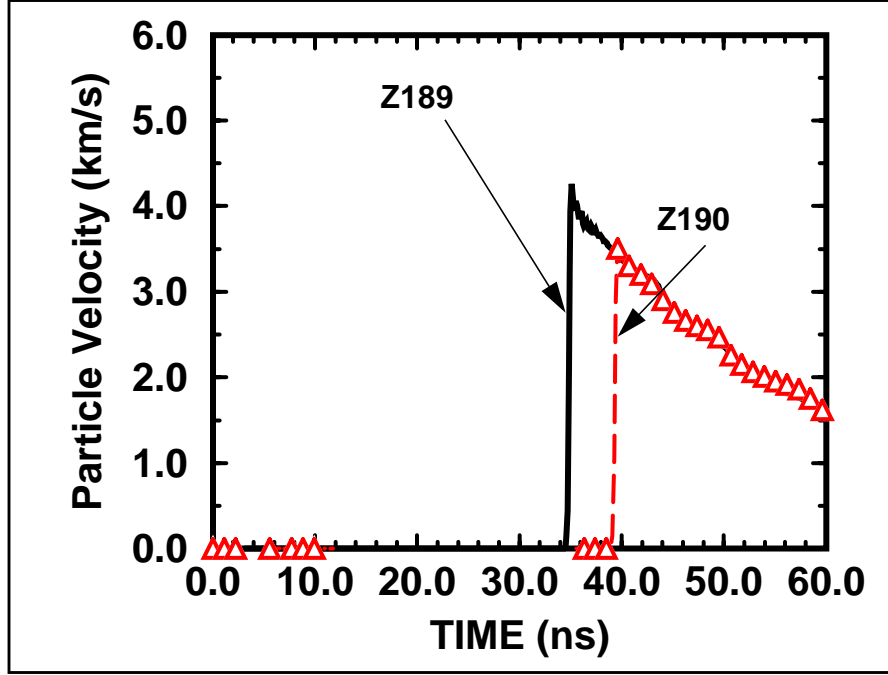


Figure 37. Z189B versus Z190B. Triangles are the ALEGRA calculation corresponding to Z190.

As a second comparison, we return to the issue of dealing with the experimental indeterminacy of the drive below the 20 to 30 eV temperature range. In our calculations, and as shown in Figure 7, we simply extrapolated the experimental drive data to 1 eV at the calculation time of zero. We test how much influence this assumption has on our particular baseline calculations for both Z189 and Z190 by starting the temperature history at its earliest measured value (about 16 eV for Z189, 25 eV for Z190 at time zero).

The comparisons with the baseline calculation in each case are shown in Figures 38 and 39. Perhaps as expected (since the time range of the difference is so small) we see very little difference in arrival time between the calculations. Perhaps more surprisingly, the difference between the calculations in the post peak amplitude regime is not negligible. The calculations with the 18 eV extrapolation move slightly closer to the experimental data. For our purposes in this report, we will only stress that this result confirms the importance of accurately measuring the early stages of the radiation pulse for experiments such as those discussed here.

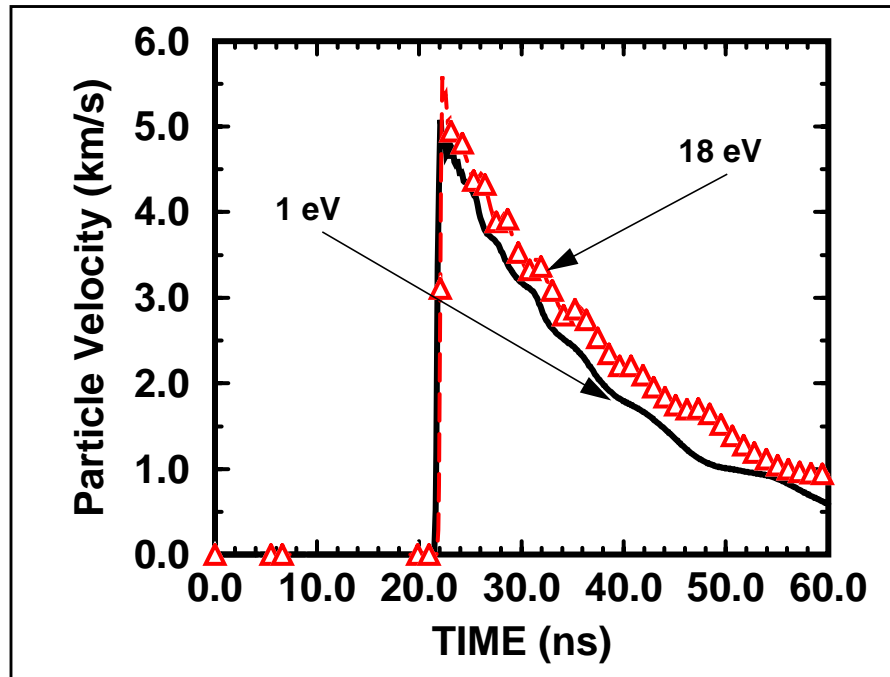


Figure 38. Baseline versus 18 eV extrapolation for Z189A. Triangles correspond to the 18 eV extrapolation in the drive.

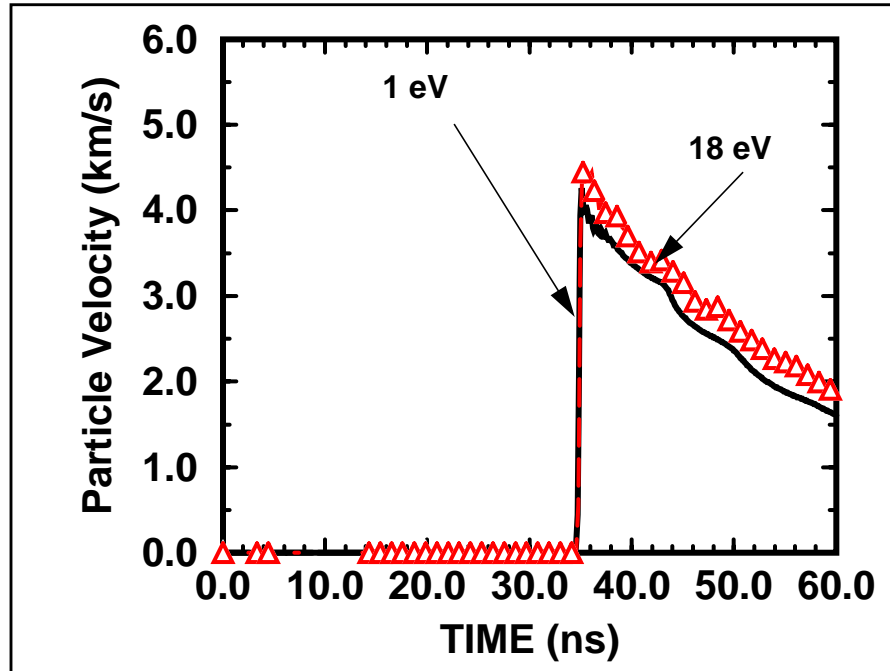


Figure 39. Baseline versus 18 eV extrapolation for Z189B. Triangles correspond to the 18 eV extrapolation in the drive.

4. Discussion

We have simulated two of the first successful experiments performed on the Sandia Z machine for the purpose of acquiring time resolved radiatively driven shock wave data. These are shot Z189 and Z190. The main reasons to perform this study are:

- Careful analysis of the experiments provides insight into the design of future experiments, as well as better understanding of the information contained in the data.
- The data potentially provide a source of validation data for the radiation-hydrodynamics models used in ALEGRA.

The comparisons between calculation and experiments shown in Figures 18, 19, 28, and 29 are interesting and useful. The agreement is of reasonable accuracy, yet significant quantitative details in the experimental data are not matched. There are at least three reasons, aside from fundamental calculation inaccuracies, that could account for these differences. These are sample preheat, non-uniform drive, and inaccurate characterization of the experimental radiation drive in the calculations.

We have observed above that there is no predicted radiative preheat of the sample in either of the two experiments analyzed. Therefore, we do not believe that radiative preheat is influencing shock wave formation and propagation in the samples at the experimental depths.

It is generally anticipated that the radiative drive on the EOS samples in shots Z189 and Z190 could be non-uniform due to the nature of the radiative flux into the secondary hohlraum from the primary hohlraum, as well as the details of the emission from the secondary hohlraum walls. The above calculations and their comparison with the experimental data appear to suggest that the radiative drive in the secondary hohlraum is, indeed, not uniform across the exposed face of the sample. This was particularly striking in the experimental data comparison of Figures 28 and 29, where the data acquired at the propagation distance of 308 μm showed less steepness in the pressure wave than those acquired at 154 μm .

A full analysis of the potential for non-uniform illumination of EOS samples in tangential secondary hohlraums is not within the scope of this report. The issue is broadly discussed in Reference 20. Radiosity calculations designed to study the potential for non-uniform sample illumination in these hohlraums in a static material approximation are discussed in Reference 21. These calculations demonstrated that non-uniform illumination was, in fact, highly likely in tangential secondary hohlraums, leading to the likelihood of corruption of the VISAR data for the purpose of EOS determination. One of the most interesting results from this more detailed examination of illumination characteristics of the secondary hohlraum is that significant non-uniform illumination of the sample (enough to corrupt EOS measurements) takes place even if there is no diagnostic aperture. In other words, the overall geometry and nature of the flux from the primary is sufficient to induce non-uniformity. The longer side of the secondary hohlraum, an asymmetry induced by its

Analysis of Z Pinch Shock Wave Experiments

tangential design, is also hotter than the shorter side of the hohlraum. This is a major contributor to non-uniformity. Note that this analysis ignores radiation-hydrodynamic effects of an aperture, such as hole closure and asymmetric plasma blowoff due to the radiation pulse that could contribute more significantly to radiation imbalance in the secondary.

Further analysis of this type suggests that axial secondary hohlraums, such as those depicted in Figure 40 [22], may be considerably more uniform in their sample illumination characteristics. (We have also included other ideas for non-axial secondary hohlraums in this figure.) However, they are also more likely to be subject to preheat effects, especially from the hard component of the Z-pinch X-ray pulse, as well as from possible highly energetic electron emission during the pinch collapse. There is now some experimental evidence that this is exactly the case [23], a subject for further discussion in the future.

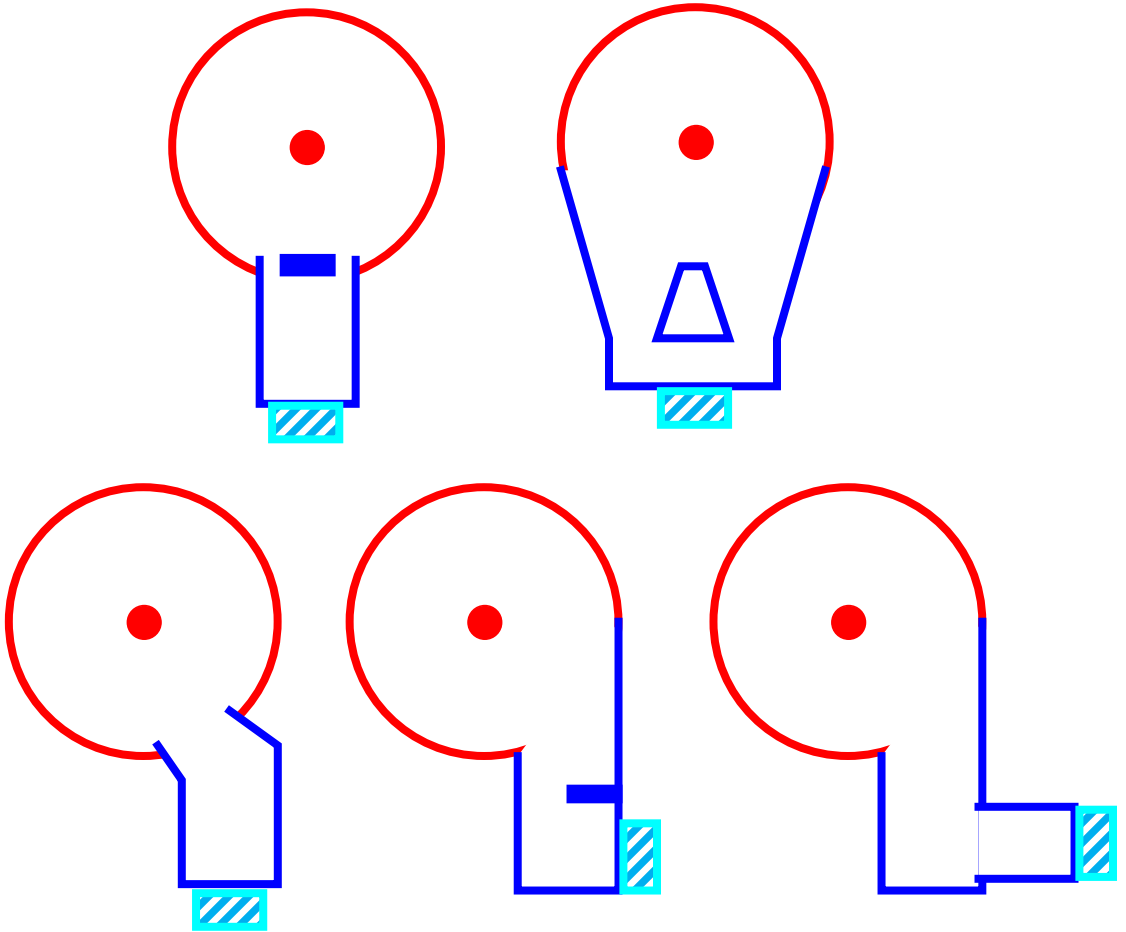


Figure 40. Possible hohlraum geometries of interest for EOS experiments.

Recent data confirm the radiosity calculations and our thoughts on preheat when using hohlraums that directly view the stagnated z-pinch. Fiber optically coupled shock arrival sensors that detect changes in surface reflectivity upon shock arrival have been used to infer

Analysis of Z Pinch Shock Wave Experiments

shock profiles resulting from different secondary hohlraum geometries. Hohlraum configurations have been designed for use on Z which allow useful regions up to approximately 3mm in diameter with acceptable shock uniformity. In addition, a paralyne preheat foil thickness has been determined and demonstrated to remove sample preconditioning to within the sensitivity of the VISAR for these configurations. These results will be the subject of a future report.

We conclude by mentioning that there are two major caveats in the calculations presented in this report. First, we have not performed detailed multi-dimensional calculations (see Appendix A). These are essential for better exploring potential inhomogeneities associated with the drive conditions in secondary hohlraums of the type used in these experimental studies. Such calculations will be the objective of subsequent work, but are well beyond the scope of the present computational study.

Second, we have not included electron thermal conduction in these calculations. Thus, we have not analyzed the possibility of electron conduction preheat at the experimental data collection depths. This is probably not a problem, for aluminum and at the Planckian temperatures that were present in the current experiments. Nonetheless, the study has not been performed. Also, we must continue to refine our understanding of how Planckian this drive really is.

Given the basic assumptions and constraints stated in the body of the report, the greatest uncertainty in the calculation is the radiation drive characterization. Details of the drive below an effective 30 eV Planckian threshold are unavailable for these experiments. The error bars around the drive data are also difficult to characterize. The effective Planckian unfolding from the original spectrally resolved data, as well as difficult calibrations associated with diagnostic hole closure dynamics, influence the accuracy of the drives given in Figures 5 and 6. It is generally believed that the peak drive temperatures in these figures are lower than actually occurred, perhaps by as much as 10 eV, due to the lack of a correction for hole closure and time-dependent albedo. Since our predictions consistently slightly overestimate the peak particle velocity observed in the VISAR data, a more accurate drive characterization may increase the error in our comparisons with the data. This is one reason why we need to be careful about the conclusions we draw from the good agreement between calculation and experiment presented in this report.

In conclusion we note three distinct directions for further investigation in the future. First, we would like to examine mechanisms for refining the generated shock wave to be more suitable for purposes of EOS measurements. Two possibilities of interest are the use of low density CH foams in the payload to reduce the attenuation of the generated shockwave, and the use of the radiative drive to launch a condensed phase flyer plate for use as an impactor. Second, we would like to perform a more detailed investigation of the sensitivity of the experimental EOS data to a wider class of radiative drive variations. Finally, we would like to establish protocols and refine experimental data accuracy to better enable the use of similar experiments for validating the radiation-hydrodynamics codes used in the Sandia Z pinch program.

References

1. D. D. Ryutov, M. S. Derzon, and M. K. Matzen (1998), "The Physics of Fast Z Pinches," Sandia National Laboratories Report, SAND98-1632.
2. R. B. Spielman, C. Deeney, G. A. Chandler, M. R. Douglas, D. L. Fehl, M. K. Matzen, D. H. McDaniel, T. J. Nash, J. L. Porter, T. W. L. Sanford, J. F. Seamen, W. A. Stygar, K. W. Struve, S. P. Breeze, J. S. McGurn, J. A. Torres, D. M. Zagar, T. L. Gilliland, D. O. Jobe, J. L. McKenney, R. C. Mock, M. Vargas, T. Wagoner, D. L. Peterson (1998), "Tungsten Wire-Array Z-Pinch Experiments at 200 TW and 2 MJ," Phys. Plasmas, VOL. 5, No. 5, 2105-2111.
3. R. M. Summers, J. S. Peery, M. W. Wong, E. S. Hertel, Jr., T. G. Trucano, and L. C. Chhabildas (1996), "Recent Progress In ALEGRA Development and Application to Ballistic Impacts", in Proceedings of the 1996 Hypervelocity Impact Symposium, to be published in International Journal of Impact Engineering.
4. J. R. Asay, C. A. Hall, C. H. Konrad, K. G. Holland, K. J. Fleming, W. M. Trott, G. A. Chandler, L. C. Chhabildas (1998), "VISAR and Shock Breakout Experiments on Z," unpublished Sandia National Laboratories Internal Memorandum.
5. L. M. Barker and R. E. Hollenbach (1974), "Laser Interferometer for Measuring Velocities of Any Reflecting Surface," J. Appl. Phys., Vol. 45, 4872-4887.
6. L. C. Chhabildas (1987), "Survey of Diagnostic Tools Used in Hypervelocity Impact Studies," Int. J. Impact Engng., Vol. 5, 205-220.
7. R. E. Chrien (1998), private communication.
8. K. S. Holian, ed. (1984), "T-4 Handbook of Material Properties Data Bases, Vol. 1c: Equations of State," Los Alamos National Laboratory, LA-10160-MS.
9. R. L. Bowers and J. R. Wilson (1991), *Numerical Modeling In Applied Physics and Astrophysics*, Jones and Bartlett Publishers, Boston.
10. G. L. Olson (1998), "Introduction to Radiation Transport," Los Alamos National Laboratory, LA-UR-98-3353.
11. G. C. Pomraning (1973), *The Equations of Radiation Hydrodynamics*, Pergamon Press, Oxford.
12. E. W. Larsen, J. M. McGhee, and J. E. Morel (1993), "Asymptotic Derivation of the Simplified P_N Equations," Proceedings of the Joint International Conference on Mathematical Methods and Supercomputing in Nuclear Applications, 19-23 April, 1993, Kongresszentrum, Karlsruhe, Germany, Vol. I, p. 718.
13. J. E. Morel (1993), "The SP_N Equations for Radiative Transfer With Material-Motion Corrections," Los Alamos National Laboratory preprint.
14. Michael L. Hall (1998), "Spartan/Augustus Overview: Simplified Spherical Harmonics and Diffusion for Unstructured Hexahedral Lagrangian Meshes", Shavano Working Group presentation, LA-UR-98-3766.

Analysis of Z Pinch Shock Wave Experiments

15. Michael L. Hall and Jim E. Morel (1996), "A Second-Order Cell-Centered Diffusion Differencing Scheme for Unstructured Hexahedral Lagrangian Meshes", in Proceedings of the 1996 Nuclear Explosives Code Developers Conference (NECDC), UCRL-MI-124790, pages 359-375, San Diego, CA, October 21--25 1996, LA-CP-97-8.
16. Michael L. Hall and Jim E. Morel (1998), "Diffusion Discretization Schemes in Augustus: A New Hexahedral Symmetric Support Operator Method", in Proceedings of the 1998 Nuclear Explosives Code Development Conference (NECDC), San Diego, CA, October 25-30 1998, LA-UR-98-3146.
17. J. E. Morel, E. W. Larsen, and M. K. Matzen (1985), "A Synthetic Acceleration Scheme for Radiative Diffusion Calculations," J. Quant. Spectrosc. Radiat. Transfer, Vol. 34, No. 3, 243-261.
18. G. Pollack (1990), "Detailed Physics of the XSN-U Opacity Package," Los Alamos National Laboratory Report, LA-UR-90-2423.
19. T. D. Blacker (1988), "FASTQ User's Manual Version 1.2," Sandia National Laboratories, SAND88-1326.
20. J. R. Asay, C. A. Hall, C. H. Konrad, W. M. Trott, G. A. Chandler, K. J. Fleming, K. G. Holland, L. C. Chhabildas, T. A. Mehlhorn, R. Vesey, and T. G. Trucano (1998), "Use of Z-Pinch Sources for High-Pressure Equation-of-State Studies," Sandia National Laboratories draft manuscript.
21. R. A. Vesey (1998), "Radiosity Simulations for Z189-190 EOS Experiments," unpublished Sandia National Laboratories Internal Memorandum.
22. M. R. Douglas (1998), private communication.
23. J. R. Asay (1998), private communication.
24. R. A. Vesey (1998), "Revised Lightscape simulations of the Z189-190 hohlraum geometry," unpublished Sandia National Laboratories Internal Memorandum.

Appendix A: Preliminary Two-Dimensional Analysis of Shot Z189

Analysis provided by Vesey [14] clearly suggests that the radiation drive under consideration here was non-uniform across the exposed surfaces of the samples. In fact, it was not only non-uniform but also asymmetric. Thus to truly model the radiation drive and the subsequent target response would require a full three-dimensional calculation, which really is beyond the scope of this effort. However, to provide a rough first-cut estimate of the potential effects of this non-uniformity, we did run a simplified two-dimensional analog to shot Z189. Of necessity, the mesh was not nearly as fine for this calculation as for the one-dimensional problems. For our approximation we chose to look at a semi-infinite rectangular slab, which was only 650 μm thick in the direction of shock propagation. This was represented by 40 zones, growing geometrically in size, at a ratio of 1.04, from $\sim 6.8 \mu\text{m}$ to $\sim 31 \mu\text{m}$. The non-infinite lateral dimension of the slab was 6 mm, which is similar to the diameter of the actual experimental sample. The mesh in this coordinate direction was set up with 20 zones, each 300 μm wide. This leads to a zonal aspect ratio of about 44 at the front and 9.5 at the back. This mesh is far from ideal, but was required to keep the total run time within reasonable bounds. Five different temperature histories were applied over four zones each of the 20-zone boundary to represent the non-uniform radiative drive on Z189. The temperature histories were scaled from those described earlier, with the peak temperature values derived from Vesey's calculations across a sample diameter. The peak values ranged from 64.4 to 70.4 eV. (Later analysis [24] suggests that these temperatures should be higher by about 5 to 15 percent, but because the calculated pressures and velocities are relative only to themselves, the basic conclusions will not change, and the calculation was not rerun.)

The results of this calculation are shown in the accompanying figures. Figure 41 shows pressure histories for the indicated distances from the front surface, where the multiple curves are for different positions across the finite lateral dimension of the slab. Similarly, Figure 42 plots velocity histories for the two Lagrangian points where VISAR measurements were taken on shot Z189. Again, the multiple curves represent different points across lateral dimension of the slab. Because of the coarse mesh, direct comparison with the earlier one-dimensional runs on shot Z189 is not possible, mainly because the peak output values are not adequately resolved. In fact, the poor numerical resolution yields velocities that are about one-third of those calculated earlier. However, the relative amplitudes do give a reasonable indication of the importance of the drive non-uniformity. We see that the pressures vary by about 20 percent, and that the velocities differ by roughly 13 percent. The smaller variation in the velocities is due to an additional integration (smoothing) relative to the pressures.

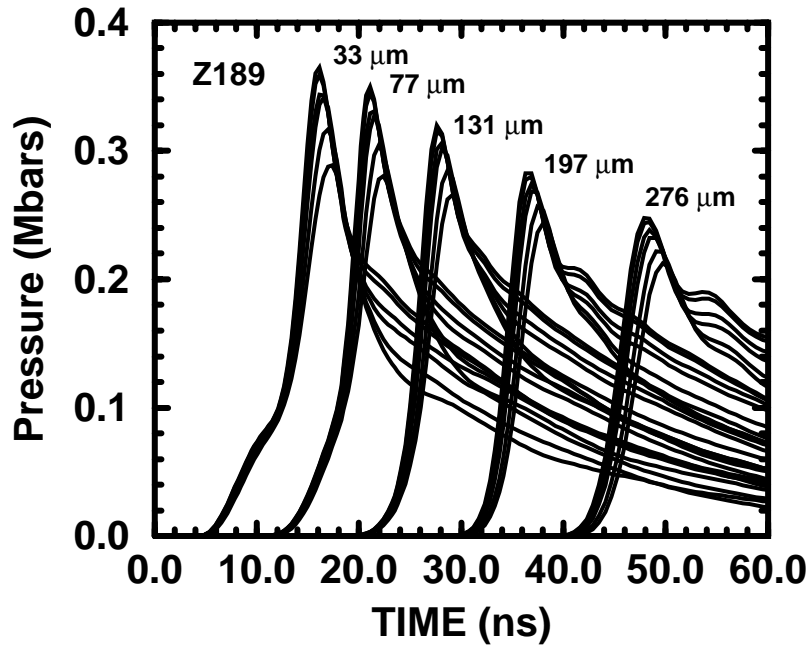


Figure 41. Calculated two-dimensional pressure histories for shot Z189. The indicated positions are the Lagrangian distances from the original front surface, and the multiple curves are for positions across the finite lateral dimension of the semi-infinite slab.

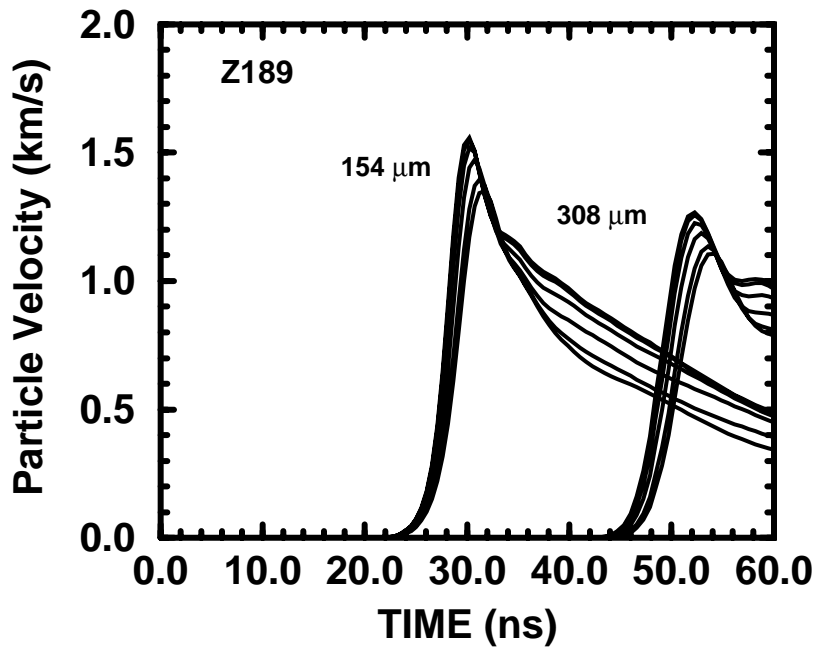


Figure 42. Calculated two-dimensional velocity histories for shot Z189 for Lagrangian points 154 and 308 (m from the original front surface). The multiple curves are for different positions across the finite lateral dimension of the semi-infinite slab.

Analysis of Z Pinch Shock Wave Experiments

The rectangular geometry used in this 2-D calculation does not give a complete picture of the true multi-dimensional response of the samples, but it does suggest bounds on the problem. These discrepancies are not large, but they are probably too large to justify the use of this specific experimental configuration for high-quality equation of state measurements. However, the overall experimental technique holds great promise for accessing new and unique parametric regimes, and we should continue to seek arrangements and/or configurations that will improve the uniformity of loading.

Appendix B - FASTQ and ALEGRA Input Listings

Listings for Z189

FASTQ input file:

```
TITLE
z189-1: 8.0E-2 Al, SP1(0.03-6.0)20; Z189-smoothed
POINT 1 0.0000000E+00 0.0000000E+00
POINT 2 5.0000000E-3 0.0000000E+00
POINT 3 5.0000000E-3 1.0000000E-2
POINT 4 0.0000000E+00 1.0000000E-2
POINT 5 8.0000000E-2 0.0000000
POINT 6 8.0000000E-2 1.0000000E-2
LINE 1 STR 1 2 0 40 1.050
LINE 2 STR 2 3 0 1 1.0000
LINE 3 STR 4 3 0 40 1.050
LINE 4 STR 4 1 0 1 1.0000
LINE 5 STR 2 5 0 300 1.0000
LINE 6 STR 5 6 0 1 1.0000
LINE 7 STR 3 6 0 300 1.0000
REGION 1 1 -1 -2 -3 -4
REGION 2 1 -5 -6 -7 -2
SCHEME 0 M
BODY 1 2
NODEBC 1 1 5
NODEBC 2 6
NODEBC 3 7 3
NODEBC 4 4
ELEMBC 1 1 5
ELEMBC 2 6
ELEMBC 3 7 3
ELEMBC 4 4
EXIT
```

ALEGRA-SPARTAN input file:

```
title
z189-1: 8.0E-2 Al, SP1(0.03-6.0)20; Z189-smoothed

physics: radiation hydrodynamics

cartesian

exodus version one

MAXIMUM INITIAL TIME STEP 1.e-12

termination time 60.0E-9

emit output: time = 1.0E-9, from 0.0 to 1.0
emit plot: time = 1.0E-10, from 0.0 to 1.0

$pisces hourglass control
$ viscosity 0.05
$end
```

Analysis of Z Pinch Shock Wave Experiments

\$pronto artificial viscosity by default

plot variable
artificial viscosity
position
velocity
energy
pressure : avg
temperature : avg
density : avg
radiation temperature
end

time step scale:
hydro 1.0
\$ strain softening 0.9
end

no displacement: nodeset 1 y
no displacement: nodeset 3 y

block 1
lagrangian mesh
material 1
end

material 1 AL
model = 1
model = 2
density 2.700 \$g/cm3
temperature 300.0 \$kelvin
end

model 1 sesame
neos = 3715
end

radiation parameters

\$energy group specification
group bounds
linear 0.00001 to 0.001 by 2
log 0.001 to 6. by 18
end

\$SP method order
SP 1
spartan robust 1 \$ 1 turns on the robust solver
\$ diffusion solver scheme 7
spartan output mode 1
spartan timestep norm 2
spartan timestep change 1.
\$ spartan timestep damping 10.

\$Boundary condition specifications (must be one for each
boundary in the problem!)
reflective boundary, sideset 1

Analysis of Z Pinch Shock Wave Experiments

vacuum boundary, sideset 2
reflective boundary, sideset 3
source boundary, sideset 4, function 1, scale 1.0E-3

\$SPARTAN control parameters

TEMPERATURE FLOOR 1.0E-5
TEMPERATURE FLOOR DT 0.01
spartan output mode 1

end

\$source temperatures must be in keV

\$ Shot Z189 (tickled slightly)

\$Time (ns) Tr (eV)

function 1

0.0	1.0
0.9E-9	16.1958
1.1E-9	17.9982
1.3E-9	19.4692
1.5E-9	19.1138
1.7E-9	16.5534
1.9E-9	17.3078
2.1E-9	18.2951
2.3E-9	21.2922
2.5E-9	21.442
2.7E-9	21.482
2.9E-9	22.1579
3.1E-9	23.0834
3.3E-9	24.211
3.5E-9	25.5179
3.7E-9	28.6705
3.9E-9	28.7212
4.1E-9	29.0627
4.3E-9	29.1342
4.5E-9	29.4104
4.7E-9	29.5249
4.9E-9	30.093
5.1E-9	30.7177
5.3E-9	31.3639
5.5E-9	31.3984
5.7E-9	31.8054
5.9E-9	32.8025
6.1E-9	33.5588
6.3E-9	34.5935
6.5E-9	36.0111
6.7E-9	37.733
6.9E-9	39.3448
7.1E-9	41.09
7.3E-9	43.2358
7.5E-9	45.7308
7.7E-9	48.0426
7.9E-9	50.2332
8.1E-9	52.5653
8.3E-9	54.9617
8.5E-9	57.2484
8.7E-9	59.3829
8.9E-9	61.4949
9.1E-9	63.5419

Analysis of Z Pinch Shock Wave Experiments

9.3E-9	65.4097
9.5E-9	67.1153
9.7E-9	68.7487
9.9E-9	70.2958
10.1E-9	71.7353
10.3E-9	73.0602
10.5E-9	74.2681
10.7E-9	75.4433
10.9E-9	76.5305
11.1E-9	77.522
11.3E-9	78.4386
11.5E-9	79.2723
11.7E-9	79.9953
11.9E-9	80.5973
12.1E-9	81.1129
12.3E-9	81.5236
12.5E-9	81.8184
12.7E-9	81.9934
12.9E-9	82.0805
13.1E-9	82.0809
13.3E-9	81.99
13.5E-9	81.8164
13.7E-9	81.5718
13.9E-9	81.2692
14.1E-9	80.9296
14.3E-9	80.5473
14.5E-9	80.154
14.7E-9	79.7415
14.9E-9	79.289
15.1E-9	78.8059
15.3E-9	78.3309
15.5E-9	77.8633
15.7E-9	77.4023
15.9E-9	76.9371
16.1E-9	76.479
16.3E-9	76.025
16.5E-9	75.5693
16.7E-9	75.1339
16.9E-9	74.7352
17.1E-9	74.3417
17.3E-9	73.9123
17.5E-9	73.5004
17.7E-9	73.1142
17.9E-9	72.7378
18.1E-9	72.3295
18.3E-9	71.9012
18.5E-9	71.511
18.7E-9	71.1082
18.9E-9	70.6746
19.1E-9	70.2645
19.3E-9	69.8658
19.5E-9	69.4684
19.7E-9	69.0356
19.9E-9	68.602
20.1E-9	68.1872
20.3E-9	67.797
20.5E-9	67.3949
20.7E-9	66.9864
20.9E-9	66.5718

Analysis of Z Pinch Shock Wave Experiments

21.1E-9	66.141
21.3E-9	65.7294
21.5E-9	65.3427
21.7E-9	64.9924
21.9E-9	64.6008
22.1E-9	64.2025
22.3E-9	63.7967
22.5E-9	63.3831
22.7E-9	62.9418
22.9E-9	62.5274
23.1E-9	62.1308
23.3E-9	61.7025
23.5E-9	61.2656
23.7E-9	60.8052
23.9E-9	60.3875
24.1E-9	59.9769
24.3E-9	59.5871
24.5E-9	59.1665
24.7E-9	58.6942
24.9E-9	58.303
25.1E-9	57.8614
25.3E-9	57.4833
25.5E-9	57.1003
25.7E-9	56.7089
25.9E-9	56.3384
26.1E-9	55.9774
26.3E-9	55.652
26.5E-9	55.3427
26.7E-9	55.0554
26.9E-9	54.6564
27.1E-9	54.3426
27.3E-9	54.0523
27.5E-9	53.685
27.7E-9	53.3418
27.9E-9	52.9298
28.1E-9	52.5385
28.3E-9	52.1845
28.5E-9	51.8281
28.7E-9	51.4598
28.9E-9	51.1293
29.1E-9	50.8339
29.3E-9	50.4262
29.5E-9	50.0903
29.7E-9	49.6886
29.9E-9	49.3848
30.1E-9	49.0464
30.3E-9	48.6605
30.5E-9	48.2456
30.7E-9	47.9603
30.9E-9	47.751
31.1E-9	47.4754
31.3E-9	47.2043
31.5E-9	46.936
31.7E-9	46.7787
31.9E-9	46.5575
32.1E-9	46.2745
32.3E-9	46.042
32.5E-9	45.8293
32.7E-9	45.5122

Analysis of Z Pinch Shock Wave Experiments

32.9E-9	45.1474
33.1E-9	44.7867
33.3E-9	44.4165
33.5E-9	44.0635
33.7E-9	43.5506
33.9E-9	43.1788
34.1E-9	42.8106
34.3E-9	42.3201
34.5E-9	41.9154
34.7E-9	41.6466
34.9E-9	41.1913
35.1E-9	40.6917
35.3E-9	40.1846
35.5E-9	39.7359
35.7E-9	39.3427
35.9E-9	38.8895
36.1E-9	38.583
36.3E-9	38.3129
36.5E-9	37.7633
36.7E-9	37.1912
36.9E-9	36.7571
37.1E-9	36.378
37.3E-9	36.0307
37.5E-9	35.8853
37.7E-9	35.8575
37.9E-9	35.6313
38.1E-9	35.1949
38.3E-9	34.7567
38.5E-9	34.6554
38.7E-9	34.3762
38.9E-9	34.2697
39.1E-9	34.1535
39.3E-9	34.0433
39.5E-9	33.5312
39.7E-9	33.0638
39.9E-9	32.808
40.1E-9	32.7135
40.3E-9	32.1044
40.5E-9	31.5104
40.7E-9	31.2258
40.9E-9	30.979
41.1E-9	30.809
41.3E-9	30.4658
41.5E-9	30.2019
41.7E-9	29.7551
41.9E-9	29.7165
42.1E-9	29.1605
42.3E-9	29.1404
42.5E-9	29.4043
42.7E-9	29.7506
42.9E-9	29.6892
43.1E-9	29.3646
43.3E-9	29.6474
43.5E-9	30.1668
43.7E-9	30.5329
43.9E-9	30.242
44.1E-9	30.342
44.3E-9	30.7061
44.5E-9	30.0285

Analysis of Z Pinch Shock Wave Experiments

44.7E-9	29.2507
44.9E-9	29.073
45.1E-9	29.368
45.3E-9	28.777
45.5E-9	28.1892
45.7E-9	27.8638
45.9E-9	28.0011
46.1E-9	28.3418
46.3E-9	27.8196
46.5E-9	27.4796
46.7E-9	27.7187
46.9E-9	27.4609
47.1E-9	24.3199
47.3E-9	21.7122
47.5E-9	18.9273
47.7E-9	16.1358
47.9E-9	13.083
48.1E-9	9.96721
48.3E-9	7.46614
48.5E-9	5.43638
48.7E-9	2.68481
48.9E-9	1.99641
49.1E-9	1.99641
49.3E-9	4.21728
49.5E-9	6.38374
49.7E-9	6.38374
49.9E-9	6.38374
50.1E-9	8.20011
50.3E-9	8.20011
50.5E-9	8.20011
50.7E-9	9.97387
50.9E-9	8.05181
51.1E-9	8.05181
51.3E-9	5.83094
51.5E-9	4.97234
51.7E-9	6.63481
51.9E-9	9.45247
52.1E-9	10.1919
52.3E-9	11.8867
52.5E-9	14.004
52.7E-9	12.2302
52.9E-9	13.874
53.1E-9	16.2027
53.3E-9	18.2046
53.5E-9	16.8968
53.7E-9	15.2343
53.9E-9	13.8292
54.1E-9	13.6458
54.3E-9	13.4873
54.5E-9	13.9037
54.7E-9	15.9966
54.9E-9	14.3528
55.1E-9	14.5243
55.3E-9	14.4324
55.5E-9	16.075
55.7E-9	16.075
55.9E-9	16.7082
56.1E-9	14.3358
56.3E-9	12.7994

Analysis of Z Pinch Shock Wave Experiments

```
56.5E-9    10.2658
56.7E-9    8.17291
56.9E-9    9.33917
57.1E-9    6.83901
57.3E-9    4.92894
57.5E-9    3.28638
57.7E-9    3.28638
57.9E-9    1.24061
58.1E-9    1.24061
58.3E-9    3.72368
58.5E-9    6.15194
58.7E-9    8.57941
58.9E-9    9.39761
59.1E-9    11.5475
59.3E-9    11.5475
59.5E-9    11.5475
59.7E-9    13.3975
59.9E-9    14.975
60.1E-9    14.975
60.3E-9    12.4919
60.5E-9    10.0637
60.7E-9    7.63621
60.9E-9    5.65174
61.0E-9    3.50188
end
```

model 2 xsn \$aluminum

number of elements 1

```
$ element 4, mass 9.01218, fraction 1.0 $beryllium
  element 13, mass 26.98154, fraction 1.0 $aluminum
$ element 26, mass 55.847, fraction 1.0 $iron
$ element 42, mass 95.94, fraction 1.0 $molybdenum
$ element 82, mass 207.2, fraction 1.0 $lead
$ element 92, mass 238.029, fraction 1.0 $uranium
$ element 79, mass 196.9665, fraction 1.0 $gold
$ element 74, mass 183.85, fraction 1.0 $tungsten
$ element 78, mass 195.09, fraction 1.0 $platinum
$ element 54, mass 131.3, fraction 1.0 $xenon
end
end
```

exit

Listings for Z190

FASTQ input file:

```
TITLE
z190-1: 8.0E-2 Al, SP1(0.03-6.0)20; Z190-smoothed
POINT 1 0.0000000E+00 0.0000000E+00
POINT 2 5.0000000E-3 0.0000000E+00
```

Analysis of Z Pinch Shock Wave Experiments

```

POINT 3 5.0000000E-3 1.0000000E-2
POINT 4 0.0000000E+00 1.0000000E-2
POINT 5 8.0000000E-2 0.0000000
POINT 6 8.0000000E-2 1.0000000E-2
LINE 1 STR 1 2 0 40 1.050
LINE 2 STR 2 3 0 1 1.0000
LINE 3 STR 4 3 0 40 1.050
LINE 4 STR 4 1 0 1 1.0000
LINE 5 STR 2 5 0 300 1.0000
LINE 6 STR 5 6 0 1 1.0000
LINE 7 STR 3 6 0 300 1.0000
REGION 1 1 -1 -2 -3 -4
REGION 2 1 -5 -6 -7 -2
SCHEME 0 M
BODY 1 2
NODEBC 1 1 5
NODEBC 2 6
NODEBC 3 7 3
NODEBC 4 4
ELEMBC 1 1 5
ELEMBC 2 6
ELEMBC 3 7 3
ELEMBC 4 4
EXIT

```

ALEGRA-SPARTAN input file:

title

z190-1: 8.0E-2 Al, SP1(0.03-6.0)20; Z190-smoothed

physics: radiation hydrodynamics

cartesian

exodus version one

MAXIMUM INITIAL TIME STEP 1.e-12

termination time 60.0E-9

emit output: time = 1.0E-9, from 0.0 to 1.0

emit plot: time = 1.0E-10, from 0.0 to 1.0

\$pisces hourglass control

\$ viscosity 0.05

\$end

\$pronto artificial viscosity by default

plot variable

artificial viscosity

position

velocity

energy

pressure : avg

temperature : avg

density : avg

radiation temperature

Analysis of Z Pinch Shock Wave Experiments

```
end

time step scale:
  hydro 1.0
$ strain softening 0.9
end

no displacement: nodeset 1 y
no displacement: nodeset 3 y

block 1
  lagrangian mesh
  material 1
end

material 1    AL
  model = 1
  model = 2
  density 2.700 $g/cm3
  temperature 300.0 $kelvin
end

model 1 sesame
  neos = 3715
end

radiation parameters

$energy group specification
  group bounds
    linear 0.00001 to 0.001 by 2
    log 0.001 to 6. by 18
  end

$SP method order
  SP 1
  spartan robust 1 $ 1 turns on the robust solver
$ diffusion solver scheme 7
  spartan output mode 1
  spartan timestep norm 2
  spartan timestep change 1.
$ spartan timestep damping 10.

$Boundary condition specifications (must be one for each
$boundary in the problem!)
  reflective boundary, sideset 1
  vacuum boundary, sideset 2
  reflective boundary, sideset 3
  source boundary, sideset 4, function 1, scale 1.0E-3

$SPARTAN control parameters

  TEMPERATURE FLOOR 1.0E-5
  TEMPERATURE FLOOR DT 0.01
  spartan output mode 1

end
```

Analysis of Z Pinch Shock Wave Experiments

\$source temperatures must be in keV

function 1 \$ Shot Z190 (tickled slightly)

0.0	1.0
0.86E-9	24.21
1.06E-9	24.119
1.26E-9	23.668
1.46E-9	23.858
1.66E-9	23.778
1.85E-9	23.34
2.05E-9	23.532
2.25E-9	23.884
2.45E-9	23.942
2.65E-9	24.158
2.84E-9	24.241
3.04E-9	23.868
3.24E-9	23.894
3.44E-9	23.64
3.65E-9	23.661
3.85E-9	24.335
4.05E-9	24.383
4.25E-9	24.326
4.45E-9	24.326
4.66E-9	24.919
4.86E-9	25.354
5.06E-9	25.861
5.26E-9	26.586
5.46E-9	27.108
5.66E-9	27.499
5.86E-9	28.073
6.06E-9	28.656
6.26E-9	29.394
6.45E-9	30.215
6.65E-9	30.869
6.85E-9	31.701
7.05E-9	32.649
7.25E-9	33.319
7.44E-9	34.116
7.64E-9	35.163
7.84E-9	36.357
8.04E-9	37.618
8.25E-9	38.808
8.45E-9	40.163
8.65E-9	41.622
8.85E-9	43.176
9.05E-9	44.86
9.26E-9	46.577
9.46E-9	48.234
9.66E-9	49.94
9.86E-9	51.498
10.05E-9	52.977
10.25E-9	54.492
10.45E-9	56.009
10.65E-9	57.517
10.85E-9	58.93
11.04E-9	60.301
11.24E-9	61.627
11.44E-9	62.924
11.64E-9	64.22
11.84E-9	65.458

Analysis of Z Pinch Shock Wave Experiments

12.04E-9	66.678
12.24E-9	67.871
12.44E-9	68.999
12.64E-9	70.039
12.85E-9	71.026
13.05E-9	71.947
13.25E-9	72.789
13.45E-9	73.549
13.65E-9	74.202
13.86E-9	74.775
14.06E-9	75.261
14.26E-9	75.645
14.46E-9	75.943
14.65E-9	76.167
14.85E-9	76.319
15.05E-9	76.393
15.25E-9	76.385
15.45E-9	76.286
15.64E-9	76.143
15.84E-9	75.944
16.04E-9	75.703
16.24E-9	75.423
16.45E-9	75.103
16.65E-9	74.756
16.85E-9	74.398
17.05E-9	73.998
17.25E-9	73.6
17.46E-9	73.202
17.66E-9	72.786
17.86E-9	72.361
18.06E-9	71.924
18.26E-9	71.487
18.46E-9	71.045
18.66E-9	70.597
18.86E-9	70.165
19.06E-9	69.757
19.25E-9	69.347
19.45E-9	68.944
19.65E-9	68.556
19.85E-9	68.171
20.05E-9	67.795
20.24E-9	67.428
20.44E-9	67.097
20.64E-9	66.769
20.84E-9	66.442
21.05E-9	66.126
21.25E-9	65.817
21.45E-9	65.492
21.65E-9	65.194
21.85E-9	64.922
22.06E-9	64.63
22.26E-9	64.329
22.46E-9	64.014
22.66E-9	63.696
22.85E-9	63.34
23.05E-9	62.995
23.25E-9	62.666
23.45E-9	62.333
23.65E-9	61.982

Analysis of Z Pinch Shock Wave Experiments

23.84E-9	61.603
24.04E-9	61.24
24.24E-9	60.879
24.44E-9	60.505
24.64E-9	60.096
24.84E-9	59.753
25.04E-9	59.372
25.24E-9	58.955
25.44E-9	58.563
25.65E-9	58.147
25.85E-9	57.773
26.05E-9	57.409
26.25E-9	57.056
26.45E-9	56.701
26.66E-9	56.371
26.86E-9	55.978
27.06E-9	55.586
27.26E-9	55.27
27.45E-9	54.933
27.65E-9	54.561
27.85E-9	54.168
28.05E-9	53.76
28.25E-9	53.36
28.44E-9	52.996
28.64E-9	52.66
28.84E-9	52.346
29.04E-9	52.002
29.25E-9	51.639
29.45E-9	51.323
29.65E-9	51.058
29.85E-9	50.776
30.05E-9	50.502
30.26E-9	50.211
30.46E-9	49.918
30.66E-9	49.622
30.86E-9	49.307
31.06E-9	48.998
31.26E-9	48.744
31.46E-9	48.441
31.66E-9	48.187
31.86E-9	47.953
32.05E-9	47.654
32.25E-9	47.42
32.45E-9	47.141
32.65E-9	46.859
32.85E-9	46.616
33.04E-9	46.48
33.24E-9	46.197
33.44E-9	45.887
33.64E-9	45.602
33.85E-9	45.392
34.05E-9	45.186
34.25E-9	44.892
34.45E-9	44.674
34.65E-9	44.499
34.86E-9	44.224
35.06E-9	43.839
35.26E-9	43.588
35.46E-9	43.408

Analysis of Z Pinch Shock Wave Experiments

35.65E-9	43.12
35.85E-9	42.781
36.05E-9	42.461
36.25E-9	42.174
36.45E-9	41.85
36.64E-9	41.555
36.84E-9	41.304
37.04E-9	41.14
37.24E-9	40.895
37.44E-9	40.646
37.64E-9	40.404
37.84E-9	40.186
38.04E-9	39.959
38.24E-9	39.708
38.45E-9	39.423
38.65E-9	38.988
38.85E-9	38.761
39.05E-9	38.49
39.25E-9	38.295
39.46E-9	37.993
39.66E-9	37.758
39.86E-9	37.522
40.06E-9	37.35
40.25E-9	37.187
40.45E-9	37.018
40.65E-9	37.094
40.85E-9	37.002
41.05E-9	36.782
41.24E-9	36.529
41.44E-9	36.392
41.64E-9	36.164
41.84E-9	35.983
42.05E-9	35.734
42.25E-9	35.576
42.45E-9	35.572
42.65E-9	35.268
42.85E-9	35.012
43.06E-9	34.984
43.26E-9	34.853
43.46E-9	34.607
43.66E-9	34.445
43.86E-9	34.212
44.06E-9	34.026
44.26E-9	33.61
44.46E-9	33.476
44.66E-9	33.244
44.85E-9	32.892
45.05E-9	32.472
45.25E-9	32.186
45.45E-9	31.999
45.65E-9	31.625
45.84E-9	31.485
46.04E-9	31.362
46.24E-9	31.338
46.44E-9	31.098
46.65E-9	31.238
46.85E-9	31.085
47.05E-9	30.792
47.25E-9	30.549

Analysis of Z Pinch Shock Wave Experiments

47.45E-9	30.503
47.66E-9	30.58
47.86E-9	30.341
48.06E-9	30.23
48.26E-9	30.269
48.46E-9	30.198
48.66E-9	29.827
48.86E-9	29.704
49.06E-9	29.937
49.26E-9	29.794
49.45E-9	29.634
49.65E-9	29.388
49.85E-9	29.28
50.05E-9	28.937
50.25E-9	28.696
50.44E-9	28.528
50.64E-9	28.579
50.84E-9	28.563
51.04E-9	28.149
51.25E-9	28.047
51.45E-9	28.096
51.65E-9	28.535
51.85E-9	28.723
52.05E-9	28.822
52.26E-9	28.858
52.46E-9	28.588
52.66E-9	28.324
52.86E-9	28.159
53.05E-9	28.471
53.25E-9	28.401
53.45E-9	28.165
53.65E-9	27.746
53.85E-9	27.533
54.04E-9	27.38
54.24E-9	27.142
54.44E-9	27.192
54.64E-9	27.143
54.84E-9	27.093
55.04E-9	27.077
55.24E-9	26.862
55.44E-9	26.9
55.64E-9	26.71
55.85E-9	26.696
56.05E-9	26.271
56.25E-9	25.887
56.45E-9	25.485
56.65E-9	25.409
56.86E-9	25.42
57.06E-9	24.771
57.26E-9	24.648
57.46E-9	24.343
57.65E-9	24.429
57.85E-9	24.178
58.05E-9	24.227
58.25E-9	24.519
58.45E-9	24.696
58.64E-9	24.53
58.84E-9	24.637
59.04E-9	25.058

Analysis of Z Pinch Shock Wave Experiments

end

model 2 xsn \$aluminum

number of elements 1

\$ element 4, mass 9.01218, fraction 1.0 \$beryllium

element 13, mass 26.98154, fraction 1.0 \$aluminum

\$ element 26, mass 55.847, fraction 1.0 \$iron

\$ element 42, mass 95.94, fraction 1.0 \$molybdenum

\$ element 82, mass 207.2, fraction 1.0 \$lead

\$ element 92, mass 238.029, fraction 1.0 \$uranium

\$ element 79, mass 196.9665, fraction 1.0 \$gold

\$ element 74, mass 183.85, fraction 1.0 \$tungsten

\$ element 78, mass 195.09, fraction 1.0 \$platinum

\$ element 54, mass 131.3, fraction 1.0 \$xenon

end

end

exit

DISTRIBUTION:

EXTERNAL DISTRIBUTION

Anderson, Charles E.
Southwest Research Institute
P.O. Drawer 28510
San Antonio, TX 78284

Kedar D. Pyatt
Systems Division, Maxwell Technologies
8888 Balboa Ave., San Diego, CA 92123

University of New Mexico
Dept. of Chemistry and Nuclear
Engineering
Albuquerque, New Mexico 87131

Attn: Prof. N. R. Roderick

Air Force Research Laboratory
AFRL/DEHP
3550 Aberdeen Avenue S. E.
Bldg 413
Albuquerque, New Mexico 87117-5776

Attn: T. W. Hussey
Attn: R. Peterkin

U. S. Department of Energy, HQ
DP-18
19901 Germantown Road
Germantown, MD 20874-1290

Attn: Chris Keane, DOE
Attn: Dave Crandall, DOE

Los Alamos National Laboratory
Mail Station 5000
P.O. Box 1663

Los Alamos, NM 87545

Attn: W.W. Anderson, MS P952
Attn: R. E. Chrien, MS D410
Attn: M. L. Hall, MS D409
Attn: A. Hauer, MS E526
Attn: R. S. Hixson, MS P952
Attn: B. L. Holian, MS B268
Attn: K. S. Holian, MS D413
Attn: L. G. Margolin, MS D413
Attn: J. E. Morel, MS D409
Attn: D. L. Peterson, MS B259
Attn: F. J. Swenson, MS B220

University of California
Lawrence Livermore National Laboratory
7000 East Ave.
P.O. Box 808
Livermore, CA 94550

Attn: R. C. Cauble, MS L-041
Attn: E. A. Chandler, MS L-097
Attn: G. W. Collins, MS L-481
Attn: R. J. Fortner, MS L-415
Attn: J. H. Hammer, MS L-018
Attn: N. C. Holmes, MS L-045
Attn: P. W. Rambo, MS L-015
Attn: B. A. Remington, MS L-021
Attn: L. J. Suter, MS L-031
Attn: A. Toor, MS L-041

SANDIA INTERNAL

MS 1454	K. J. Fleming, 1554 (10)
MS 1190	Don Cook, 1600
MS 1191	J. Quintenz, 1602
MS 1186	M. A. Sweeney, 1602
MS 1181	J. R. Asay, 1611 (30)
MS 1181	L. C. Chhabildas, 1611
MS 1181	K. Holland, 1611 (20)
MS 1181	C. Konrad, 1611 (20)
MS 1181	C. Hall, 1611 (20)
MS 1187	K. Matzen, 1670
MS 1194	R. B. Spielman, 1674
MS 1186	C. Deeney, 1674
MS 1186	M. R. Douglas, 1674

MS 1186	T. Mehlhorn, 1674	MS 0321	J. L. Tompkins, 9224
MS 1186	T. Haill, 1674	MS 1111	G. Heffelfinger, 9225
MS 1186	J. S. Lash, 1674	MS 1111	R. M. Fye, 9225
MS 1186	R. J. Lawrence, 1674 (20)	MS 1111	H. Hjalmarson, 9225
MS 1186	B. M. Marder, 1674	MS 1111	M. D. Rintoul, 9225
MS 1186	S. A. Slutz, 1674	MS 1111	M. Stevens, 9225
MS 1186	R. E. Vesey, 1674	MS 0441	R. Leland, 9226
MS 1196	G. Chandler, 1677 (20)	MS 1111	B. Hendrickson, 9226
MS 1221	J. S. Rottler, 9800	MS 0819	J. S. Peery, 9231
MS 1202	J. M. McGlaun, 5903	MS 0819	E. Boucheron, 9231
MS 9011	J. C. Meza, 8950	MS 0819	K. G. Budge, 9231 (20)
MS 9011	P. T. Boggs, 8950	MS 0819	D. Carroll, 9231
MS 9011	M. L. Koszykowski, 8950	MS 0819	R. Drake, 9231
MS 1110	L. J. Lehoucq, 8950	MS 0819	M. Christon, 9231
MS 9011	K. Long, 8950	MS 0819	E. S. Hertel, 9231
MS 9011	C. H. Tong, 8950	MS 0819	A. C. Robinson, 9231
MS 0841	P. Hommert, 9100	MS 0819	R. Summers, 9231
MS 0828	R. K. Thomas, 9104	MS 0819	T. G. Trucano, 9231 (20)
MS 0828	J. Moya, 9105	MS 0819	R. Weatherby, 9231
MS 0828	J. Garcia, 9106	MS 0819	M. Wong, 9231
MS 0834	A. Ratzel, 9112	MS 0820	P. Yarrington, 9232
MS 0834	M. R. Baer, 9112	MS 0820	M. Boslough, 9232
MS 0834	W. M. Trott, 9112 (20)	MS 0820	R. Brannon, 9232
MS 0835	S. N. Kempka, 9113	MS 0820	D. Crawford, 9232
MS 0825	W. H. Rutledge, 9115	MS 0820	E. Fang, 9232
MS 0825	R. Baty, 9115	MS 0820	A. Farnsworth, 9232
MS 0825	A. R. Lopez, 9115	MS 0820	M. E. Kipp, 9232
MS 0825	W. L. Oberkampf, 9115	MS 0820	S. A. Silling, 9232
MS 0321	W. J. Camp, 9200	MS 0820	P. A. Taylor, 9232
MS 0316	P. F. Chavez, 9204	MS 0439	M. Eldred, 9234
MS 0316	E. D. Gorham, 9209	MS 0439	J. Red-Horse, 9234
MS 0318	G. S. Davidson, 9215	MS 1179	Jim Lee, 15340
MS 0318	P. Heermann, 9215	MS 0899	Technical Library, 4916 (2)
MS 1111	S. S. Dosanjh, 9221	MS 0619	Review and Approval Desk, 00111 (1) for DOE/OSTI
MS 1111	S. Plimpton, 9221	MS 9018	Central Technical Files, 8940-2
MS 1111	A. Salinger, 9221		
MS 1111	J. N. Shadid, 9221		
MS 1111	R. Schmidt, 9221		
MS 1111	T. M. Smith, 9221		
MS 1110	D. Womble, 9222		
MS 1110	W. Hart, 9222		
MS 1110	S. Istrail, 9222		
MS 1110	R. Lehoucq, 9222		
MS 1110	S. Minkoff, 9222		
MS 1110	L. A. Romero, 9222		
MS 0321	A. L. Hale, 9224		
MS 0321	J. Ang, 9224		
MS 0321	R. Benner, 9224		
MS 0321	G. M. Pollock, 9224		